Seismically active structures of the Main Himalayan Thrust revealed before, during and after the 2015 Mw 7.9 Gorkha earthquake in Nepal

L B Adhikari, M Laporte, L Bollinger, J Vergne, S Lambotte, B P Koirala, M Bhattarai, C Timsina, R M Gupta, N Wendling-Vazquez, et al.

Geophysical Journal International

Geophys. J. Int. (2023) **232,** 451–471
Advance Access publication 2022 September 19
GJI Seismology

https://doi.org/10.1093/gji/ggac281

Seismically active structures of the Main Himalayan Thrust revealed before, during and after the 2015 M_w 7.9 Gorkha earthquake in Nepal

L. B. Adhikari,[1,5,2,5] M. Laporte,[3,5] L. Bollinger,[3,5] J. Vergne,[4,5] S. Lambotte,[4,5] B. P. Koirala,[1,5] M. Bhattarai,[1,5] C. Timsina,[1,5] R.M. Gupta,[1,5,5] N. Wendling-Vazquez,[3,5] D. Batteux,[1,5,3,5] H. Lyon-Caen,[5,6] Y. Gaudemer,[2,5] P. Bernard[2,5] and F. Perrier[2,5]

[1]*Department of Mines and Geology, National Earthquake Monitoring and Research Centre, 44600 Kathmandu , Nepal. E-mail: lbadhikari@hotmail.com*
[2]*Institut de Physique du Globe de Paris, Université de Paris, CNRS,* 1 *rue Jussieu* 75005 *Paris, France*
[3]*CEA, DAM, DIF, F-*91297 *Arpajon, France*
[4]*IPGS-EOST, CNRS/Université de Strasbourg, 67000 Strasbourg, France*
[5] *Institute of Earthscience, National Central University, Taipei city 115, Taiwan*
[6]*Laboratoire de Géologie, Ecole normale supérieure,* 24*, rue Lhomond,* 75005 *Paris, France*

Accepted 2022 July 11. Received 2022 June 26; in original form 2021 August 16

SUMMARY

The M_w 7.9 2015 April 25 Gorkha earthquake is the latest of a millenary-long series of large devastating Himalayan earthquakes. It is also the first time a large Himalayan earthquake and its aftershocks were recorded by a local network of seismic stations. In the 5 yr following the main shock, more than 31 000 aftershocks were located by this permanent network within the ruptured area, including 14 362 events with M_L greater than 2.5, 7 events with $M_L > 6$, including one large aftershock with M_w 7.2 on 2015 May 12. In 2020, 5 yr after the main shock, the seismicity rate along the ruptured fault segments was still about 5 times higher than the background seismicity before the Gorkha earthquake. Several bursts of earthquakes, sometimes organized in clusters, have been observed from a few days to several years after the main shock. Some of these clusters were located at the same place as the clusters that happened during the decades of interseismic stress build-up that preceded the large earthquake. They also happened in the vicinity of the high frequency seismic bursts that occurred during the main shock. These heterogeneities contribute to a persistent segmentation of the seismicity along strike, possibly controlled by geological structural complexities of the Main Himalayan Thrust fault. We suggest that these pre-2015 clusters revealed the seismo-geological segmentation that influences both the coseismic rupture and the post-seismic relaxation.

Key words: Seismic cycle; Asia; Seismicity and tectonics; Continental tectonics: compressional.

1 INTRODUCTION

The earthquake activity of central Himalayas has been monitored continuously since 1994 by the national seismological network of Nepal (NEMRC), comprising 21 seismic stations deployed in a narrow topographical band between the frontal hills and the high Himalayan summits (Fig. 1a). Most of the seismicity takes place along the downdip-end of the locked fault segments of the Main Himalayan Thrust fault (MHT), the shallow dipping mega-thrust between Indian plate and Tibetan Plateau (e.g. Pandey *et al.* 1995; Cattin & Avouac 2000; Avouac *et al.* 2001; Bollinger *et al.* 2004; Ader *et al*. 2012).

This mid-crustal seismicity exhibits significant lateral variations (Fig. 1a) including (1) a large spread of mid-crustal earthquakes in western Nepal (Pandey *et al*. 1999 ; Hoste-Colomer *et al.* 2018, Laporte *et al.* 2021), (2) a narrow and straight band of seismicity which develops below the southern slopes of the high Himalayan range in central Nepal (Pandey *et al.* 1995) and (3) a more complex zone of seismicity spread between the Moho of the India crust and mid-crustal and shallow clusters in eastern Nepal (Monsalve *et al.* 2006).

These lateral variations, illuminated by a high rate of small earthquakes (with magnitude lower than 4) and occasional light to moderate earthquakes (magnitudes between 4 and 6), were persistent during the 3 decades that followed the installation of the network.

On 2015 April 25, the large M_w 7.9 Gorkha Nepal earthquake nucleated in the central narrow band of seismicity at mid-crustal depths (10–20 km), near the villages of Barpak, Gorkha.

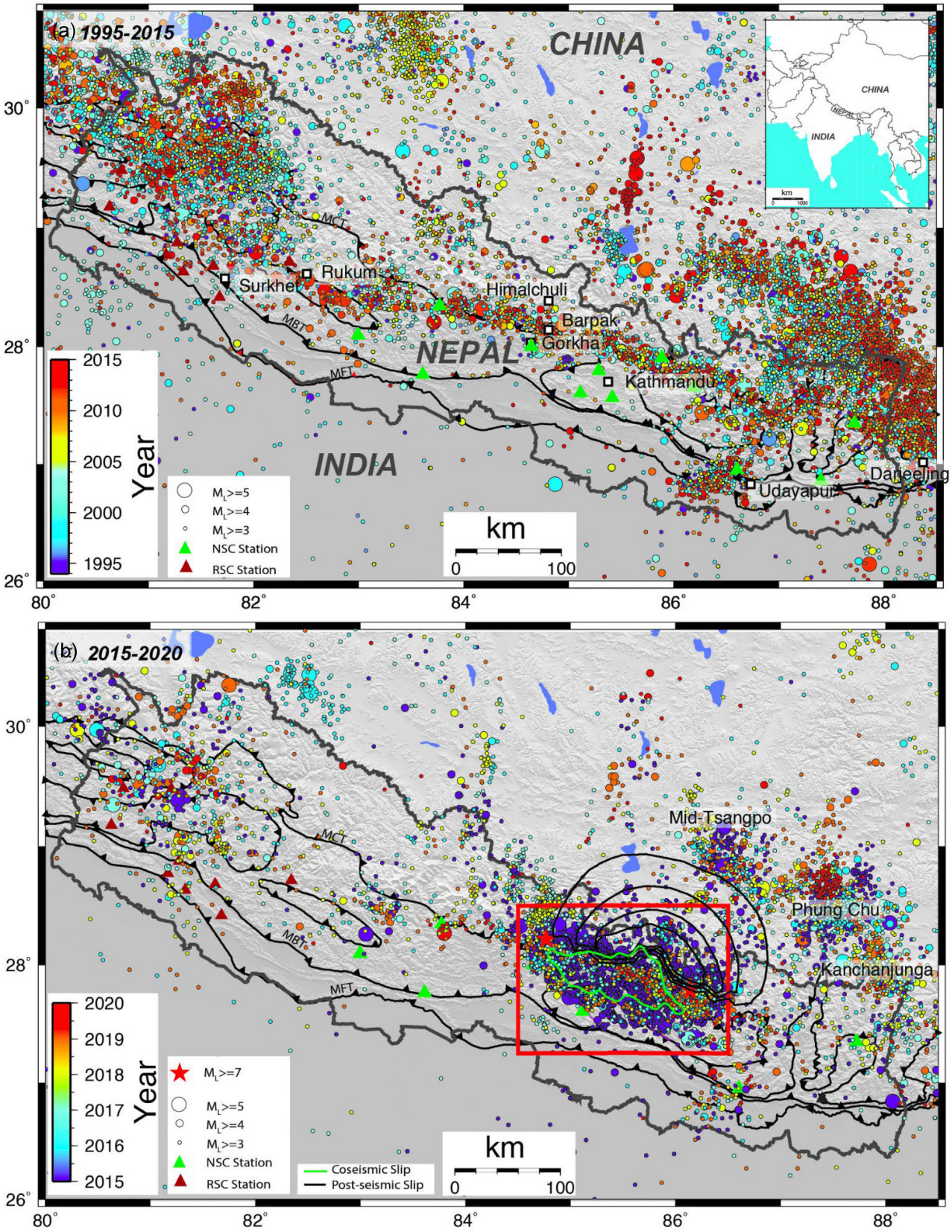

Figure 1. Seismicity maps of Nepal with the main tectonic structures. MFT, MBT, MCT stand for main frontal, boundary and central thrusts, respectively. Green and red triangles: seismic stations of the permanent networks. (a) Earthquakes epicentres located by the national seismological networks (NSC and RSC) between 1994 and 2015 April 24. (b) Earthquakes' epicentres located by the NSC between 2015 April 25 and 2020 April 25. Red rectangle localizes the region of aftershocks covered by this study. Green and blue polylines correspond respectively to the contours of coseismic (2 m contour, Grandin *et al.* 2015) and post-seismic slip (Zhao *et al.* 2017).

This is the largest earthquake that occurred in Nepal since 1934 (e.g. Sapkota *et al*. 2013 and 2016). The rupture of the 2015 earthquake propagated eastward for about 60 s during which the locked segment of the MHT was half ruptured over a 50-km-wide and 140-km-long stretch. The earthquake accommodated locally more than 5 m of coseismic slip at depth (e.g. Avouac *et al.* 2015; Denolle *et al.* 2015; Galetzka *et al.* 2015; Grandin *et al.* 2015; Kobayashi *et al.* 2015; Lindsey *et al.* 2015; Bai *et al.* 2016).

In the days following the main shock, dozens of the largest aftershocks were systematically studied at teleseismic distances (Letort *et al.* 2016; Wang *et al.* 2017), revealing some spatial heterogeneity of intermediate earthquakes realizations along the western, eastern and southern ends of the rupture (Fig. 2). This heterogeneity was attributed, and sometimes confirmed by the focal mechanisms (Fig. 2), to the presence of ramps and tear faults along the Main Himalayan Thrust fault and their spatial variations at depth (Adhikari *et al.* 2015; Letort *et al.* 2016; Wang *et al.* 2017).

Some early studies documented the temporal decay of these aftershocks that follow a modified Omori law (Adhikari *et al.* 2015) and is better apprehended by physics-based approaches (Segou & Parsons 2016). In the meantime, the behaviour of the Main Himalayan Thrust was also constrained by the GPS velocity field which helped determine the relaxation processes including the presence of a deep afterslip (Mencin *et al.* 2016; Sreejith *et al.* 2016; Gualandi *et al.* 2017; Zhao *et al.* 2017; Jouanne *et al.* 2019; Liu-Zeng *et al.* 2020; Hong & Liu 2021).

In the months after the Gorkha earthquake, several temporary seismic arrays were deployed in Nepal and southern Tibet in order to capture a well-resolved set of aftershocks (e.g. Bai *et al.* 2016; Kurashimo *et al*. 2019 ; Karplus *et al.* 2020). They confirmed that part of the seismicity that happened during the first months following the main shock is controlled by the geological structures at depth (Baillard *et al.* 2017; Hoste-Colomer *et al.* 2017; Wang *et al*. 2017 ; Bai *et al.* 2016, 2019; Mendoza *et al*. 2019; Yamada *et al.* 2020). The small earthquakes associated with these structures therefore help reveal the morphology of the fault system at depth or the mechanisms at work (e.g. Holtkamp & Brudzinski 2014; Qiu *et al.* 2016; Ross *et al.* 2020). These tectonic structures may act as receiver faults of the stress build up, barriers modulating the rupture or conduits channelizing fluids. They likely control the seismicity behaviour in the longer term.

In this study, we document a more complete set of 5 yr of aftershocks of the Gorkha earthquake recorded by the national seismological network of Nepal. These seismic records complement the early observations and capture detailed information along strike the main rupture. We present an analysis of the earthquake catalogue, exploring the spatio-temporal evolution of the aftershocks. We confront it to the earthquake activity that happened prior to the earthquake, during the interseismic period. We finally document some patterns of seismicity along the rupture that appear persistent at seismic cycle scale and may reveal the position of structures at depth controlling the segmentation of earthquakes.

2 DATA ACQUISITION AND METHODOLOGY

2.1 The NEMRC network

At the time of the Gorkha earthquake, in April 2015, the national seismological network of Nepal was composed of two independent networks: (1) an array of nine stations deployed in far-west Nepal and telemetered to the Regional Seismological Centre (RSC) in Surkhet and (2) the NEMRC network, with 12 stations deployed from west to east Nepal and transmitted to the National Earthquake Monitoring and Research Centre (NEMRC) in Kathmandu (Fig. 1).

Seismometers are installed in vaults in protected compounds. In April 2015, all sites were equipped with a short period (1 s), vertical component seismometer (ZM500). The telemetry was analogous, with digitization of the signal performed in Kathmandu at NEMRC. In May 2016, the network was upgraded to digital, with digital radio telemetry and new short-period, vertical component, 1 Hz seismometers at all sites but Kakani (KKN), Koldanda (KOLN) and Odare (ODAN), which were replaced by CMG-3T Guralp broadband three-component seismometers. Despite short (a few days) transient unavailability of some seismic stations, the geometry of the seismic network that contributed to the catalogue we describe here remained constant during the whole time period considered. For the sake of consistency, we also avoided changes in the geophysical workflow, in order to avoid biases while analysing the time structure of the seismicity. As early attempts at mixing both RSC and NEMRC seismic bulletins contributed to a significant location bias (Adhikari *et al.* 2015), we used only records from the NEMRC network to locate the earthquakes. However, we used the magnitude determined at both NEMRC and RSC stations. Indeed, the seismic signal of the largest aftershocks that happened in the core of the NEMRC stations is saturated, preventing the calculation of a local magnitude with these sole stations.

2.2 Preliminary processing

All seismic waveforms from the permanent stations of the NEMRC network were first processed using the Jade-Onyx earthquake monitoring system. Arrival times of Pg, Pn and Sg, Sn waves of the seismic events detected were picked manually by analysts. From April 2015 to April 2020, analysts at Department of Mines and Geology (DMG) manually picked 597 111 phases, mainly Pg and Sg, locating a total of 51 670 earthquakes. The seismic events are routinely located with an earthquake location algorithm (LocGSE) based on Geiger (1910) (Duverger *et al.* 2021).

The velocity model considered in the event locator is the 1D/3-layer velocity model (Pandey *et al.* 1995). Because the distribution of the seismic stations contributing to the earthquake location is rarely optimal for a good hypocentral depth determination (see Supporting Information Fig. S1), the location algorithm often fails to determine a free depth and instead assigns a fixed depth. The final depth corresponds to the one associated with the lowest RMS (e.g. Duverger *et al.* 2021).

A local magnitude M_L was determined for every event by measuring at station i the maximum amplitude [$A(i)$] of the Sg, Sn. The local magnitude M_L at NEMRC is calculated using the following equation:

$$M_L\mathrm{NEMRC}\,(i) = \log\left[A\,(i)\,/\,T\right] + B\,[\mathrm{Delta}\,(i)] + C\,(i)\,, \qquad (1)$$

where T is the period, B is the attenuation law, and $C(i)$ a station correction term. The attenuation law is expressed as a function of the epicentral distance (Delta) and includes a geometrical spreading correction and an anelastic attenuation term:

$$B(\mathrm{Delta}) = -1.85 + 0.854\,\log 10(\mathrm{Delta}) + 0.00102\,\mathrm{Delta}, \qquad (2)$$

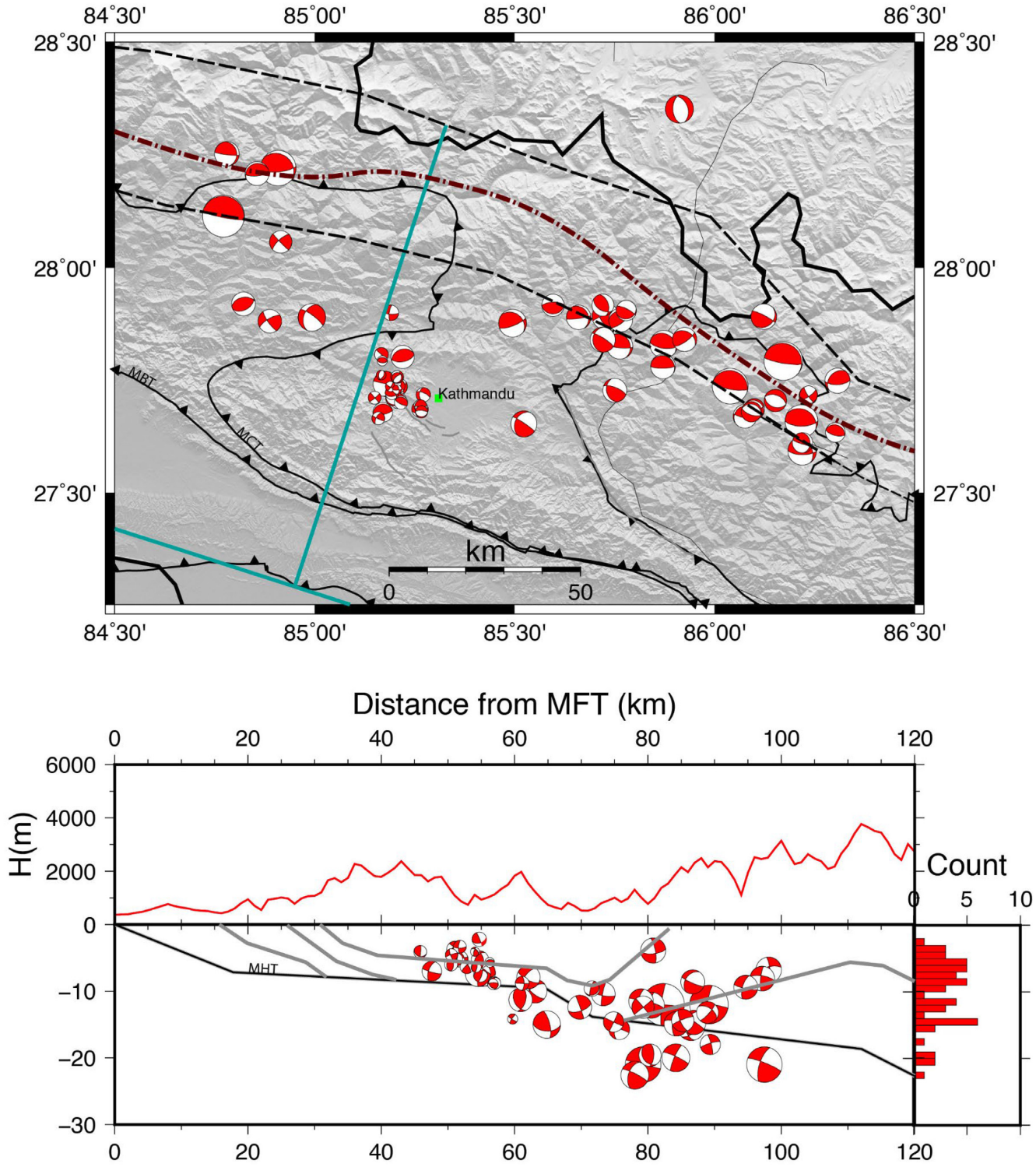

Figure 2. Focal mechanisms of Gorkha earthquake and its aftershocks (Wang *et al.* 2017; Bai *et al.* 2019; Kurashimo *et al.* 2019; Mendoza *et al.* 2019 and the GCMT). Black dashed polylines stand for the downdip limits of the coupling on MHT by Lindsey *et al.* (2018), brown dot-dashed polyline locates the base of the MHT ramp in Hubbard *et al.* (2016). (a) Map view. (b) Cross-section along the N018E dark green profile shown on the map (a).

2.3 Location refinements

In this work, we choose to only use the locations with at least 10 phase picks from the initial NEMRC bulletin. We aim first at refining the catalogue of seismic events produced at the seismic centre, using a two-step procedure. It comprises an absolute and a relative location process for the best earthquakes in the seismic bulletin. First, we select the events documented by at least 10 phase picks (11 745 out of 51 670 events) and relocated them with Hypo71 (Lee & Lahr 1972).

The velocity model we selected is the one used routinely by the NEMRC to locate events in Central Nepal (Pandey *et al.* 1995).

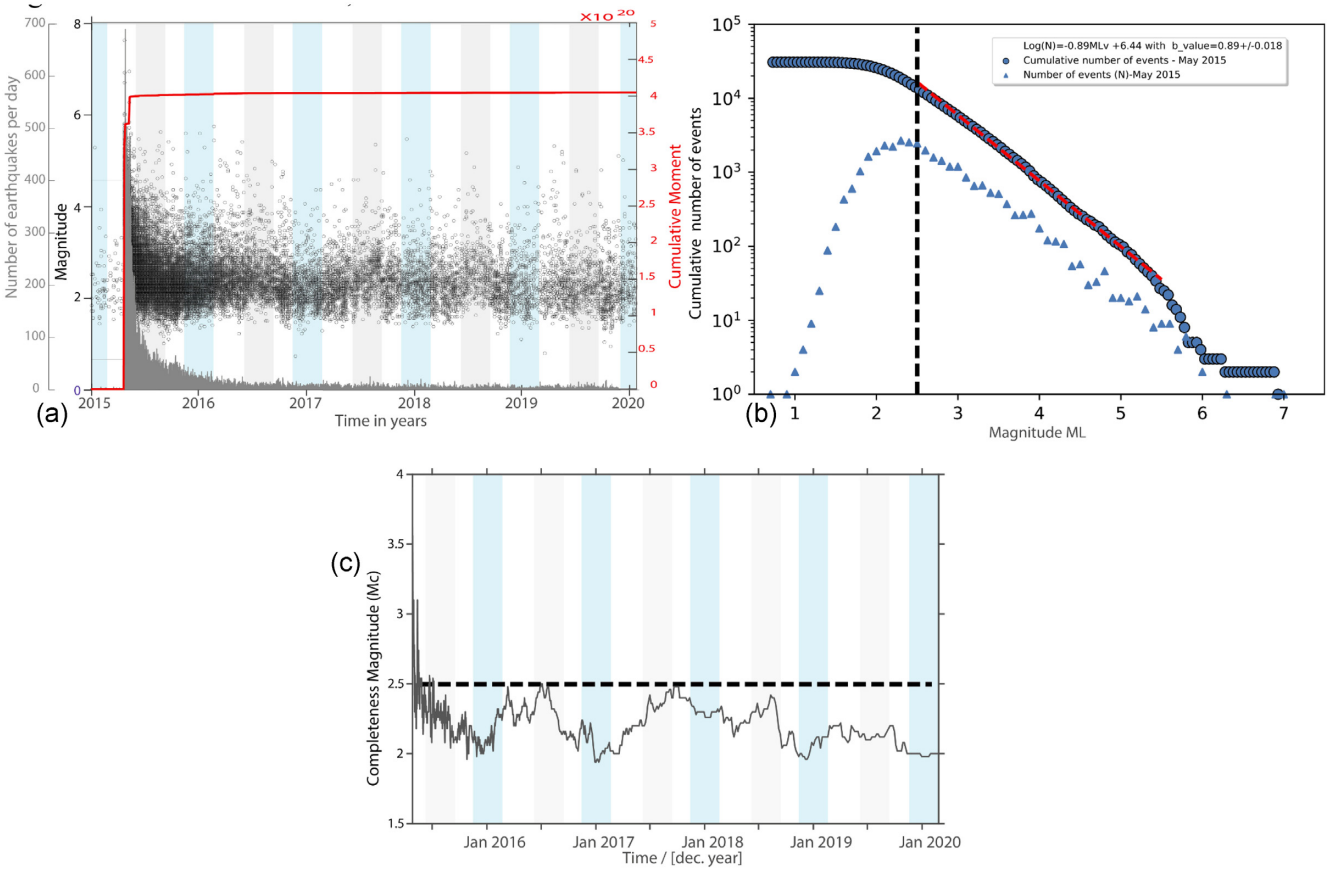

Figure 3. Earthquake magnitude distribution 2015–2020. (a) Earthquakes' time-series, magnitude distribution in M_L and cumulative moment (in 10^{20} Nm) as a function of time. Light blue and grey bars respectively represent wet and dry seasons. Note the depletion of the smallest earthquakes (around magnitude 2.0) during the wet summer monsoon period. (b) Gutenberg–Richter plot of the cumulative number of events located by NSC analyst. The straight-line portion of the curve yields a *b*-value of 0.89, while the progressive flattening of the curve below M_L 2.5 is the result of the incompleteness of the seismic catalogue below this value. Black dashed line materializes M_c 2.5. Histogram of the magnitude in blue triangles. (c) Time variations of the completeness magnitude assessed by the maximum curvature method. A set of 500 aftershocks is considered, with a magnitude bin at 0.1 and an overlapping window of 4 per cent (see Woesnner & Wiemer 2005).

However, a Wadati plot of the P and S arrival times for events located in the Kathmandu area -quiescent before the Gorkha earthquake—shows an unusually low Vp/Vs ratio around 1.68. Therefore, we decided to apply a specific model for the events in the Kathmandu cluster using Pandey *et al.* (1995) Vp model and applying a Vp/Vs ratio of 1.68 to get the Vs model.

In order to better integrate the uncertainty of picking in the location procedure, we introduced a weighting of phase picks, with a weight of 0.75 on the P and 0.25 on the S.

Because not all seismic stations contribute equally to a good hypocentral location determination, we weighted the picks as a function of the distance, with a weight of 1 when the contributing station is within 50 km and a weight of 0 above 300 km, with a linear decrease in between.

We then relocate the earthquakes by calculating their relative locations with the HypoDD software (Waldhauser & Ellsworth 2000).

This approach minimizes the residuals of traveltime differences between pairs of events recorded at a common station. It allows improving the event location by mitigating the impact of the variability of the velocity structure across Nepal but at the expense of hypocentral locations that are no longer absolute. HypoDD was applied systematically to relocate the high quality events in every individual cluster to improve the relative location of every hypocentres. The HypoDD relocations were performed independently for the 7 distinct zones of earthquake activity described in the next section. This setting was found optimal for relocating the earthquakes but created an artificial heterogeneity laterally while merging the individual catalogues.

The minimum number of links required to define a neighbour was set to 10.

We find an optimal setting of events pairing by fixing a maximum distance of 400 km between a pair of events and a station, 10 km between events constituting a pair. Each pair is defined by a maximum number of 20 neighbours per event, a minimum of 10 links and 10 phase's observations (see Supporting Information Table S3 for full description of the parameters used in HypoDD).

11 311 high quality events were selected in the 7 zones of application of the HypoDD (See Table S4), and represent the contribution of 409 632 phases picked by the analysts. We found 1 189 049 pairs of P-phases and 934 369 pairs of S-phases constituting 145 173 pairs of events with an average number of 10 links and an average offset between event's pairs between 2.6 and 3.8 km depending on the zone considered (see Supporting Information Tables S4 and S5 for the results). The use of one or the other catalogue, full original

Table 1. Summary of the seismotectonic properties of the Gorkha and Kodari earthquakes.

Earthquake		Gorkha	Kodari	Source
Date		25/04/2015	12/05/2015	NEMRC
time		06:11:24.9	07:05:20.3	
Epicentre (longitude, latitude)		84.7684, 28.2175	86.1364, 27.7849	NEMRC
Depth (km)		13.4	11.4	ISC-EHB
Moment magnitude M_w		7.9	7.2	
Seismic Moment (N m)		7.7×10^{20}		Grandin 2015
		7.2×10^{20}		Avouac 2015
		8.40×10^{20}	8.85×10^{19}	Lay 2017
		8.91×10^{20}	7.94×10^{19}	From M_w
Rupture geometry				
Length (km)		153		Grandin 2015
Width (km)		72		
Strike (°E)		285		
Average slip (m)		4		
Peak slip (m)		7		
Rupture dynamics				
Duration (s)		50		Grandin 2015
		51	22	Lay 2017
Velocity (km s^{-1})		3.1–3.3		Grandin 2015
		3.3	2.0	Lay 2017
Afterslip				
Afterslip moment 2 d		6.0×10^{18}		Gualandi 2017
Afterslip moment 7 months		1.3×10^{20}		Gualandi 2017
Afterslip 1 yr		1.0×10^{20}		Zhao 2017
Afterslip moment 1.2 yr	Nepal	$(1.21 \pm 0.15) \times 10^{20}$		Liu-Zeng 2020
	Tibet	$(2.37 \pm 0.13) \times 10^{20}$		

catalogue, Hypo71 refined catalogue of best events, or HypoDD relocated catalogue, is specified in the figure captions.

3 SPATIO-TEMPORAL VARIATIONS OF SEISMICITY

3.1 Overview of the aftershock catalogue

A total of 51 670 events were located within Nepal and adjoining regions from April 2015 to April 2020. In the trace of the Gorkha earthquake rupture and its immediate vicinity (within latitude 27.25°E to 28.5°E and longitude 84.5°N to 86.5°N), 19 270 were associated with magnitude $M_L > 2.5$ and 7567 with magnitude $M_L > 3.0$ (Fig. 3). In addition, 947 earthquakes with magnitude M_L 4.0 and above triggered the seismic alert, a magnitude threshold above which the NEMRC systematically reports the magnitude and location of the earthquake to the authorities and the public.

The rate of these earthquakes with magnitude M_L above 4 rapidly decreased within days after the occurrence of the main shock, until the occurrence of the large 2015 May 12 M_w 7.2 Kodari earthquake. This event, the second largest shock of the seismic sequence, ruptured a 30-km-long new segment of the MHT to the east of the mainshock rupture (e.g. Grandin *et al.* 2015). It was followed by many aftershocks, significantly raising the earthquake rate (Adhikari *et al.* 2015). The Gorkha and Kodari earthquakes released about all the seismic moment dissipated by the seismic crisis (Fig. 3a, Table 1). However, despite the rapid decrease of the number of aftershocks, the rate of events still appears high in 2020, higher than the rate prior to the main shock (Fig. 3a)—a result quantified in the discussion section. The period between 2015 and 2020 was affected by a progressively decreasing number of observed aftershocks in the magnitude range $2 < M_L < 5$. Below magnitude 2, the number of earthquakes shows a significant seasonal fluctuation, the earthquake catalogue being depleted of the smallest earthquakes during the summer monsoon period (Fig. 3a). This observation is not surprising as it reflects the variations of the detection capacity of the seismic network which is lower in summer than in winter (Bollinger *et al.* 2007) partly due to a higher, high-frequency seismic noise level caused by debris flows and solid and liquid transport in the rivers (Burtin *et al.* 2008; Burtin *et al.* 2009).

The completeness magnitude M_c, defined here as the magnitude above which the number of events in the catalogue is 95 per cent of the number of events anticipated by the Gutenberg–Richter straight line with a *b*-value at 0.89, is $M_c = 2.5$ (Fig. 3b). Fig. 3c illustrates the time variations of the M_c, assessed by the maximum curvature method (e.g. Woessner & Wiemer 2005). This M_c is estimated on a moving window of 500 earthquakes, with magnitude binning at 0.1, and an overlap of 4 per cent. The M_c appears seasonally modulated between 2.0 and 2.5. The lowest values are obtained in winter while the largest happen during the summer monsoon. This result is consistent with the observation of higher high frequency seismic noise during summer monsoon periods, due to rivers and landslides (e.g. Burtin *et al.* 2008, 2009).

3.2 Spatial distribution of the aftershocks

The seismicity recorded by the NEMRC network within the 5 yr following the Gorkha earthquake is mainly spread along the fault patch that ruptured during the main shocks of 2015 April 25 and May 12. Indeed, as illustrated on Fig. 4, the aftershocks are mostly localized at the periphery of the fault segments that ruptured and follow the 2 m coseismic slip isocontour. This region corresponds to the area where the coseismic slip is suspected to dampen abruptly down to 0 on the fault plane, a place where the coseismic static stress changes are the largest. The seismicity shows significant lateral

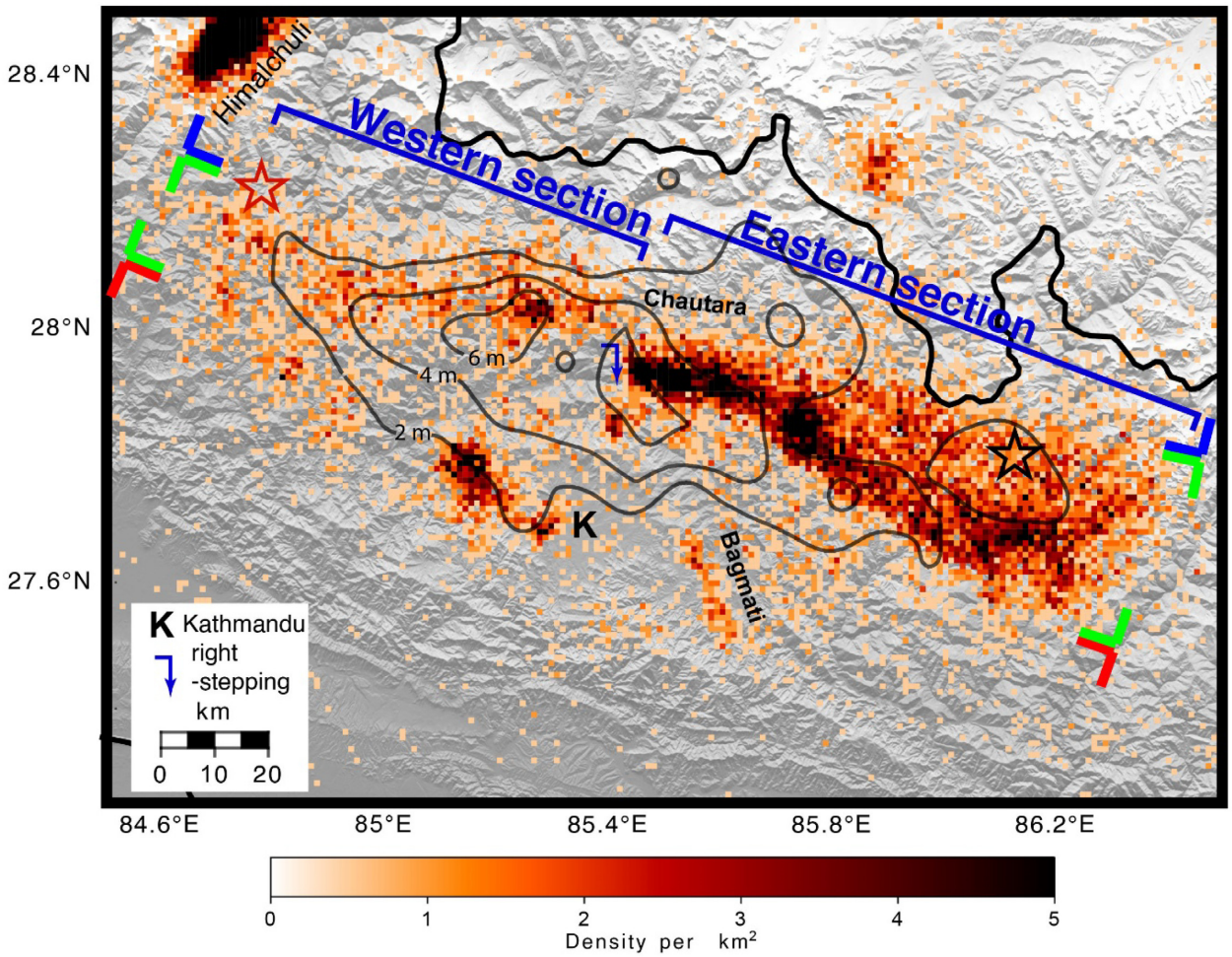

Figure 4. Density of aftershocks after the 2015 April 25 M_w 7.9 Gorkha earthquake from the full original Onyx catalogue. Density of earthquakes per km^2 is computed as the log normalized of the number of events greater than the magnitude of completeness (M_c 2.5). Red and black stars correspond respectively to the Gorkha and Kodari earthquake epicentres. Red, green and blue separators delineate the three main domains of the seismicity occurring across the rupture. These separators are used later in the text and figures (e.g. Fig. 8) for differentiating the aftershock activity.

variations, which appear more pronounced than the lateral coseismic slip variations.

At the first order, the seismicity which develops at the foot of the high range presents two distinct segments in terms of density of aftershocks. A 80-km-long western segment develops between 84.6° and 85.4°, presenting a succession of small groups of earthquakes (Fig. 4). A nearly 100-km-long eastern segment is composed of a much denser seismicity between 85.4°E and 86.4°E. Along this segment, the seismicity spreads over increasingly large widths towards the east, the seismicity spread varying from 10 to 40 km (Fig. 4). A careful examination of the density of aftershocks along both segments, let us suspect a slightly more complex smaller scale segmentation. The seismicity between the Gorkha main-shock epicentre and 85° spreads within a 10–40-km-large band of earthquakes constituted by a group of five 5–10-km-radius clusters of earthquakes. Further east, two large clusters develop in the vicinity of the western patch of maximum coseismic slip (north of the isocontour 6 m). Further East, as previously mentioned, the seismicity of the eastern section appears significantly different. First of all, there is an abrupt discontinuity in the main mid-crustal seismic cluster, whose southern edge develops 15 km more toward the south, creating a right-stepping along the mid-crustal seismic pattern. A more than 25 km-long elongated cluster, striking N105°E, develops there, in a region named 'Chautara' along the northern edge of the 4–6 m coseismic slip. Further east, three other significant 'right-stepping' discontinuities in the seismicity are visible. The most pronounced of these discontinuities falls at the corrugation of the 2 m isocontour where a 10-km-radius dense seismic cluster develops. The seismicity further east, along the northern edge of the Gorkha earthquake rupture or in the vicinity of the Kodari earthquake rupture, spreads through a wider zone, exceeding 25 km. Along the southern edge of the Gorkha earthquake coseismic rupture, the seismicity pattern appears much simpler, the aftershocks being mainly concentrated within two distinct large clusters. The largest one is located to the west of the Kathmandu valley, following the corrugated shape of the 2 m isocontour. A second narrower and more rectilinear, 20-m-long cluster, develops further east along the eastern end of the Kathmandu klippe, beyond the area affected by the rupture (Fig. 4).

Significant variations of hypocentral depths accompany the lateral aftershock epicentral variations. Indeed, the seismicity which develops along the northern edge of the rupture appears progressively shallower towards east. The depths of the earthquakes appear 5 km shallower at the eastern end than at the western end of the rupture. Although difficult to characterize, the change in average hypocentral depth could be corroborated with some of the

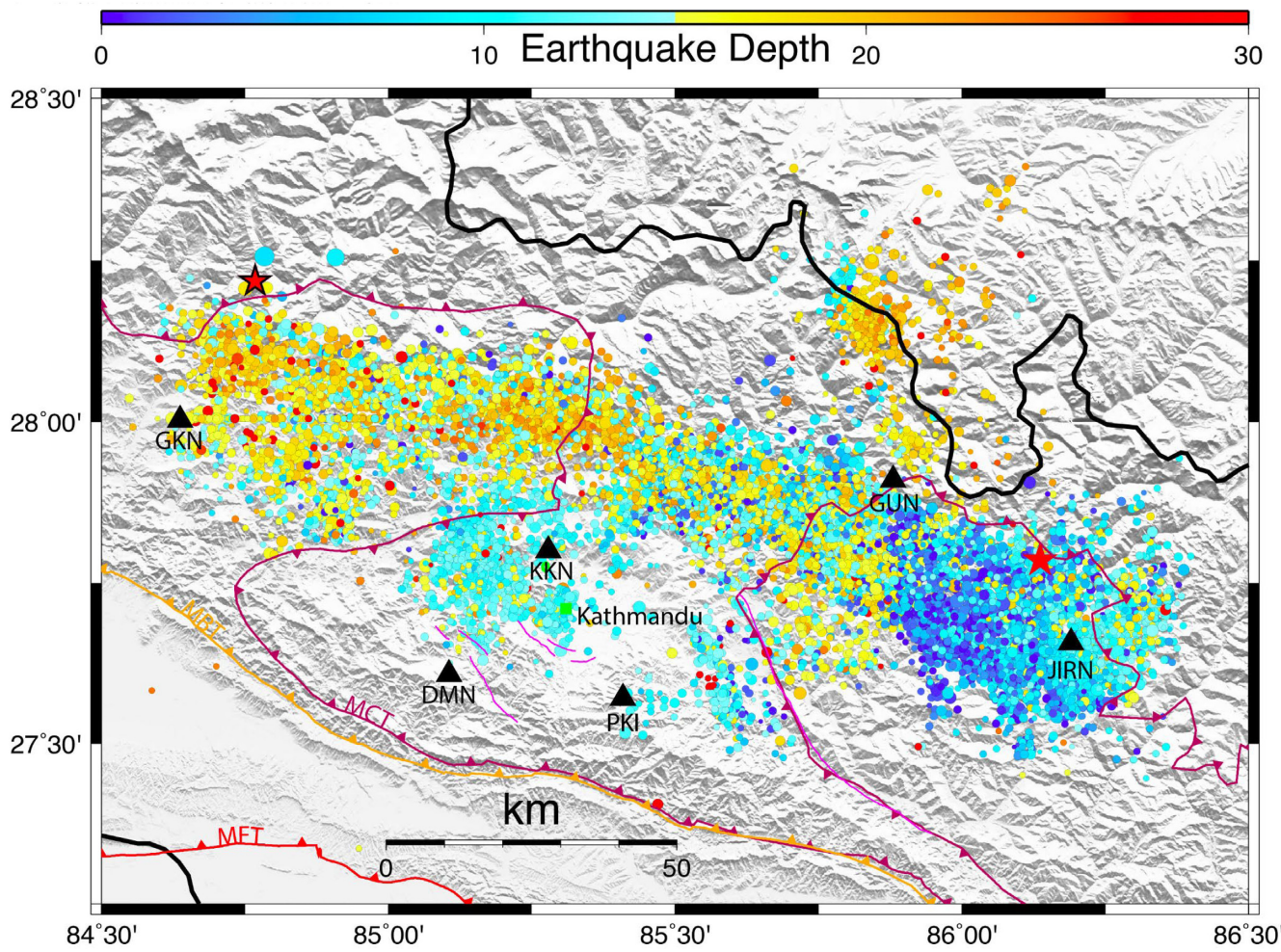

Figure 5. Seismicity map of the best located aftershocks (i.e. more than 10 seismic phases contributing to the location) with depth as the colour code. The depth is here determined using Hypo71 with a common set of parameters for all zones. Red stars correspond to the Gorkha and Kodari earthquake epicentres.

seismic segments delineated along strike. The depth of the earthquakes within the cluster at the southern edge appears also significantly shallower than those of the main cluster along the northern edge (Fig. 5).

The in-depth examination of the spatial variations of the seismicity illustrated in Figs 4 and 5, complemented by systematic analysis of the main clusters time-series, lead us to divide the aftershocks clusters into distinct regions materialized by the 'boxes' presented on the Fig. 6). Although some of the divisions may appear rather subjective, they reflect a first-order spatio-temporal segmentation of the seismicity, into distinct zones of earthquake activity marked by along-strike changes in the seismicity pattern. We used that division later to quantify systematically the seismicity pattern and its variations.

3.3 Space–time distribution of the aftershocks

The space–time distribution of all aftershocks reveals a clustering of activity within the zone ruptured by the main shock (Figs 6 and 7, and Supporting Information Figs S1 and S2).

Because the seismic clusters do not extend continuously from the downdip to the updip ends of the seismicity, we choose to divide the seismic area into three regions (delineated in Fig. 8): (1) a southern region, along the updip end of the rupture comprising the trace of the Kathmandu basin and northern Mahabharat range (red circles in Fig. 8), (2) a central region, along the downdip end covering the area devastated by the main shock (green circles on Fig. 8) and (3) a northern region beneath the High Himalayas and the southern Tibetan plateau (blue circles in Fig. 8). The temporal behaviour of the seismicity in both southern and central regions shows no significant differences: the clusters south of Kathmandu develop from the first day of the sequence, are persistent and show a temporal decay similar to the one observed for the northern clusters. At the same time, clustered seismicity developed episodically beneath the High Himalayas and Tibetan plateau. The most important of these clusters happened under the Himalchuli range between 84.5°E and 85°E (Fig. 8) and is described in details in Adhikari *et al.* (2021).

Although the rate of seismicity strongly decreased with time at the periphery of the rupture, the seismic regions that produced aftershocks in the first days after the main shock were still producing earthquakes in 2019 and 2020 (Fig. 4), despite the very low post-seismic straining along the fault surface ruptured coseismically (Fig. 4). Indeed, most of the afterslip and viscous relaxation resolved by the cGPS happened north of the downdip end of the rupture, under the High Himalaya and the Tibetan plateau (e.g. Gualandi *et al*. 2017 ; Zhao *et al.* 2017). This post-seismic straining is maximal from 85.25°E to 86.25°E along the central and eastern

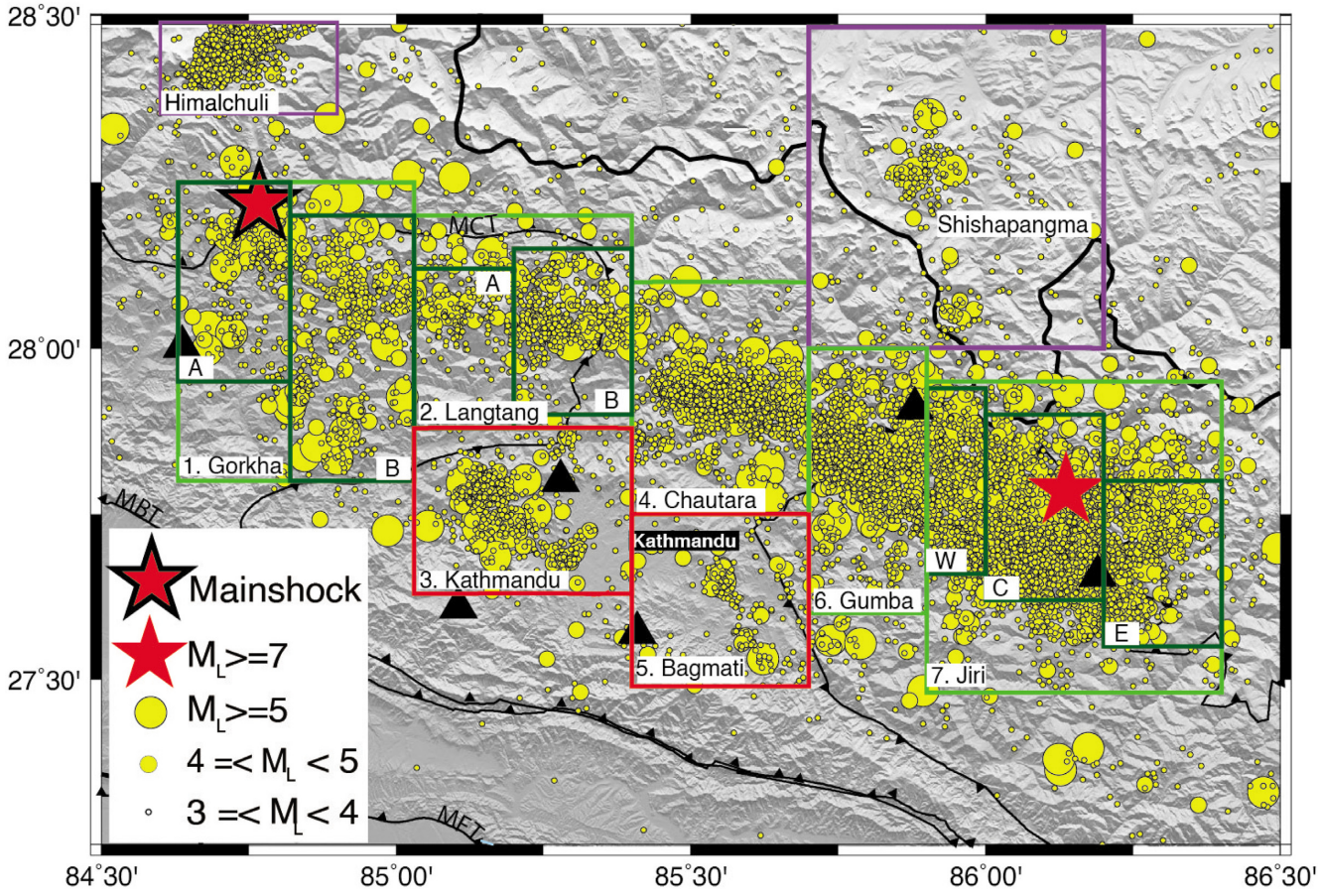

Figure 6. Map of the seismicity from 2015 April 25 to 2020 April 25 from the full original catalogue. Green rectangles delineate the extent of the zones considered in the aftershock analysis (Table 2). Subzone rectangles are also defined in the Gorkha, Langtang and Jiri zones.

trace of the region affected by the rupture, which corresponds also to the region with the largest aftershock rates.

3.4 Comparison with pre-Gorkha earthquake activity

A summary of the properties of the seismic activity is presented in Table 2 for the aftershocks, and in Supporting Information Table S1 for the preceding interseismic period. The activity associated with the Gorkha and Kodari earthquakes of 2015 appears clearly in the seismicity observed in this particular zone of Nepal (defined in Fig. 1b, excluding the Himalchuli region, see above) since the beginning of the operation of the NEMRC network (Fig. 9). Only 18 earthquakes with $M_L > 5$ were recorded from 1994 January 1 to 2015 April 24, compared with 111 aftershocks with $M_L > 5$ since 2015 April 25 (Fig. 9a). The largest earthquake, in this zone, before the Gorkha earthquake, is the 2001 July 16 M_L 5.95 earthquake ($M_w = 5.28$ ISCGEM), with an epicentre located 28.013°N, 84.878°E, about 25 km from the epicentre of the Gorkha earthquake, and an hypocentre at a 10 km (fixed) depth. The second largest is the 1997 January 31 M_L 5.82 M_w 4.84 Sarshin earthquake (Hoste-Colomer *et al.* 2017), with an epicentre north of Kathmandu (28.037°N, 85.344°E). Before the Gorkha sequence, an earthquake with M_L 5.28 occurred on 2015 January 11 (27.959°N, 85.727°E), in Sindhupalchowk, 99 and 44 km from the epicentres of the Gorkha and Kodari earthquakes, respectively. Given the background rate of occurrence of $M_L > 5$ earthquakes in the region, this earthquake cannot be considered as a convincing precursor.

In this region and since 1994, a total of 16 025 and 6820 earthquakes were recorded with $M_L > 2.5$ and $M_L > 3.0$, respectively. These numbers include 1689 and 664 earthquakes that occurred before the Gorkha earthquake. The average event rate before the Gorkha earthquake was 0.084 ± 0.5 event per day with $M_L > 3.0$ (plain grey line in Fig. 9b), with an average Seismic Moment Release Rate (SMRR) of 8.8×10^{14} Nm per period of 100 d. Regarding the interseismic event rate with $M_L > 3.0$, a small but significant difference is observed (dash-dot grey line in Fig. 9b) for the period from 1994 to 2004 (0.069 ± 0.7 d^{-1}) compared with the period from 2005 to 2015 (0.099 ± 0.8 d^{-1}). This difference could be attributed to changes that affected the network in 2005. However, while such changes could have affected the detection of local magnitudes smaller than 3.0, with the completeness magnitude of the catalogue increasing from M_L 2.0 before 2005 to M_L 2.5 after 2005 (Adhikari 2021), no clear effect could be identified able to affect magnitudes $M_L > 3.0$. In addition, a systematic bias due to the detection thresholds would not increase the event rate after 2005, but decrease it instead. Since a systematic bias can therefore be ruled out, the change in the event rate in 2005 could reflect a real change in seismicity during the interseismic period, nevertheless to be considered with caution.

5 yr after the main shocks, the event rate and the SMRR remain much higher than their respective values during the interseismic period. When considering the average values from 2017 April 25

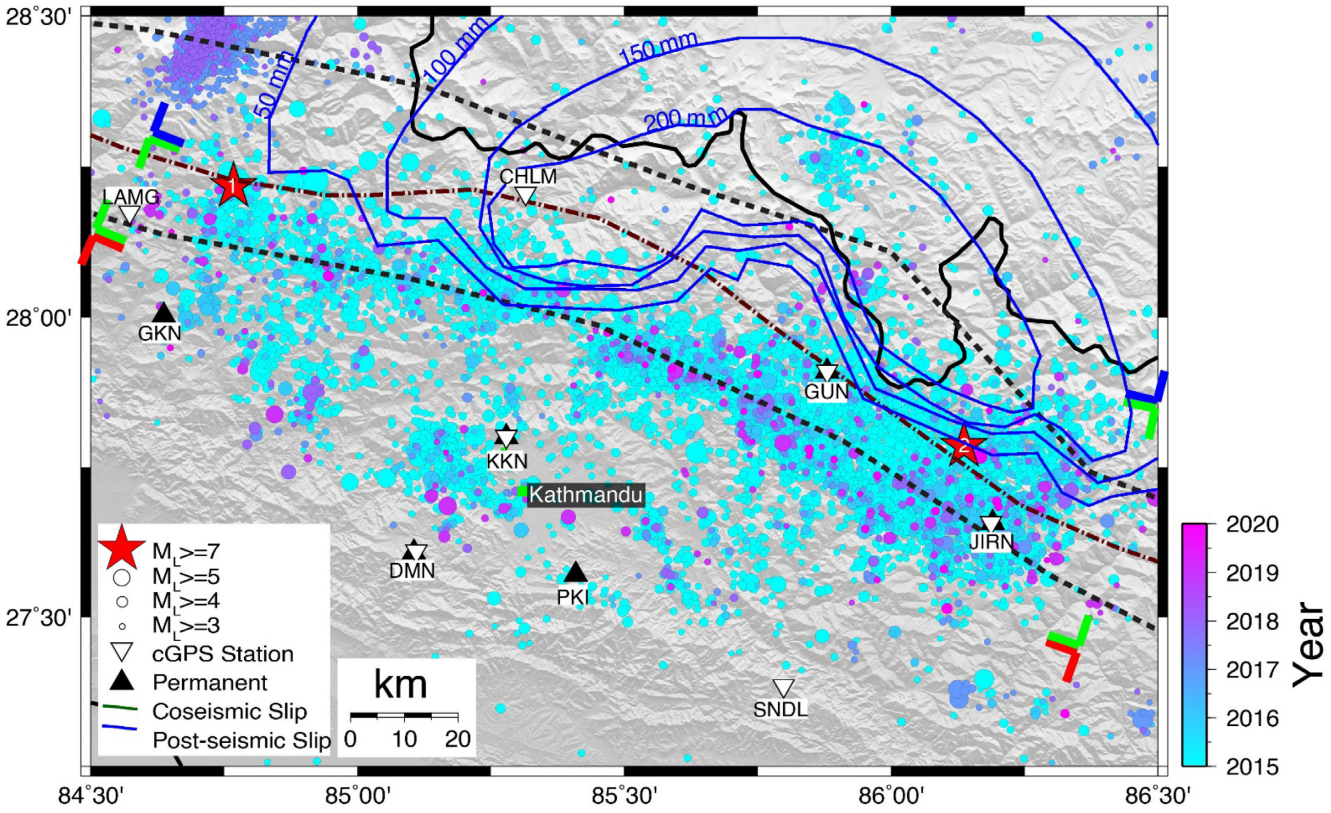

Figure 7. Seismicity map of the Gorkha earthquake rupture area and aftershocks; time colour coded. Red stars with numbers 1 and 2, respectively, represent the epicentres of the Gorkha earthquake of 2015 April 25 and the Kodari earthquake of 2015 May 12. Green, blue, brown dot-dashed and black dashed polylines: contours of coseismic slip with 2 m interval starting from 2 m, contours of afterslip with values shown in the figure, model base downdip limits of the coupling on MHT by Lindsey *et al*. (2018) and the location of the base of the MHT ramp by Hubbard *et al.* (2016). Red, green and blue separators delineate the three main domains of the seismicity occurring across the rupture. These separators are used later in the text and figures (e.g. Fig. 8) for differentiating the aftershock activity.

to 2020 April 25, the event rate is 0.39 ± 0.05 d^{-1} and the SMRR 1.13×10^{16} Nm per period of 100 d, about 4 and 13 times larger than the interseismic values.

4 RESULTS AND INTERPRETATIONS

4.1 Segmentation of seismicity along and across the rupture

As mentioned, and illustrated earlier (Fig. 4), the area affected by the seismicity shows significant lateral variations. A detailed analysis of this seismicity allows us to divide it into several distinct zones (Fig. 8).

Two zones of the High Himalayan Range and the Tibetan Plateau present a seismic pattern clearly distinct from the remaining seismic background. The first develops in the vicinity of the Himalchuli—Manaslu mountain range, a large group of very high Himalayan summits culminating at 8156 meters. This region exhibits episodic seismic swarms which developed from summer 2017 about 30 km north of the epicentre of the Gorkha earthquake. The description of this seismicity, off the main fault rupture, is the subject of another paper (Adhikari *et al* 2021) and is therefore not detailed here. The second zone covers the Shishapangma mountain range, another eight-thousander, in the vicinity of which a large seismic cluster developed (*e.g.* Li *et al.* 2017). The NEMRC network is not optimal for studying these two regions which exhibit earthquakes associated with large azimuthal gaps.

The main region affected by the aftershocks of the Gorkha earthquake, further south, can be divided into 5 main boxes (light green boxes on Fig. 6), right-stepping strands of the seismicity, 20 to 50 km wide, delimited after examining the maps of epicentres, as well as density map of earthquakes (Figs 4–6).

The first box is 40 km wide and comprises the western end of the Gorkha earthquake rupture. The seismicity there is relatively sparse, made of several distinct clusters, and may be divided into two seismic bands, the seismicity eastward being spread on a significantly longer slice (Fig. 6).

The second box covers the Kathmandu–Langtang region (Fig. 6). The northern part of the zone (Langtang area) corresponds to the downdip end of the rupture and is associated with denser seismic clustering in the east than in the west. The seismicity south of the Kathmandu region is shallower than in the north, and falls along the updip end of the main shock rupture. The next band of seismicity to the east (labelled Chautara in Fig. 6) comprises a 30-km-long N110 E mid-crustal seismic cluster clearly separated from the Langtang cluster to the NW and Gumba cluster to the East. These right-stepping seismic strands are persistent during the interseismic period, the seismicity step potentially coinciding with a 20 km tear fault (Hoste-Colomer *et al.* 2017). The Bagmati region, along the southern updip end of the rupture in the area, exhibits a seismic cluster parallel to the structural contact between the Kathmandu klippe and the Lesser Himalayas in its footwall. Contrarily

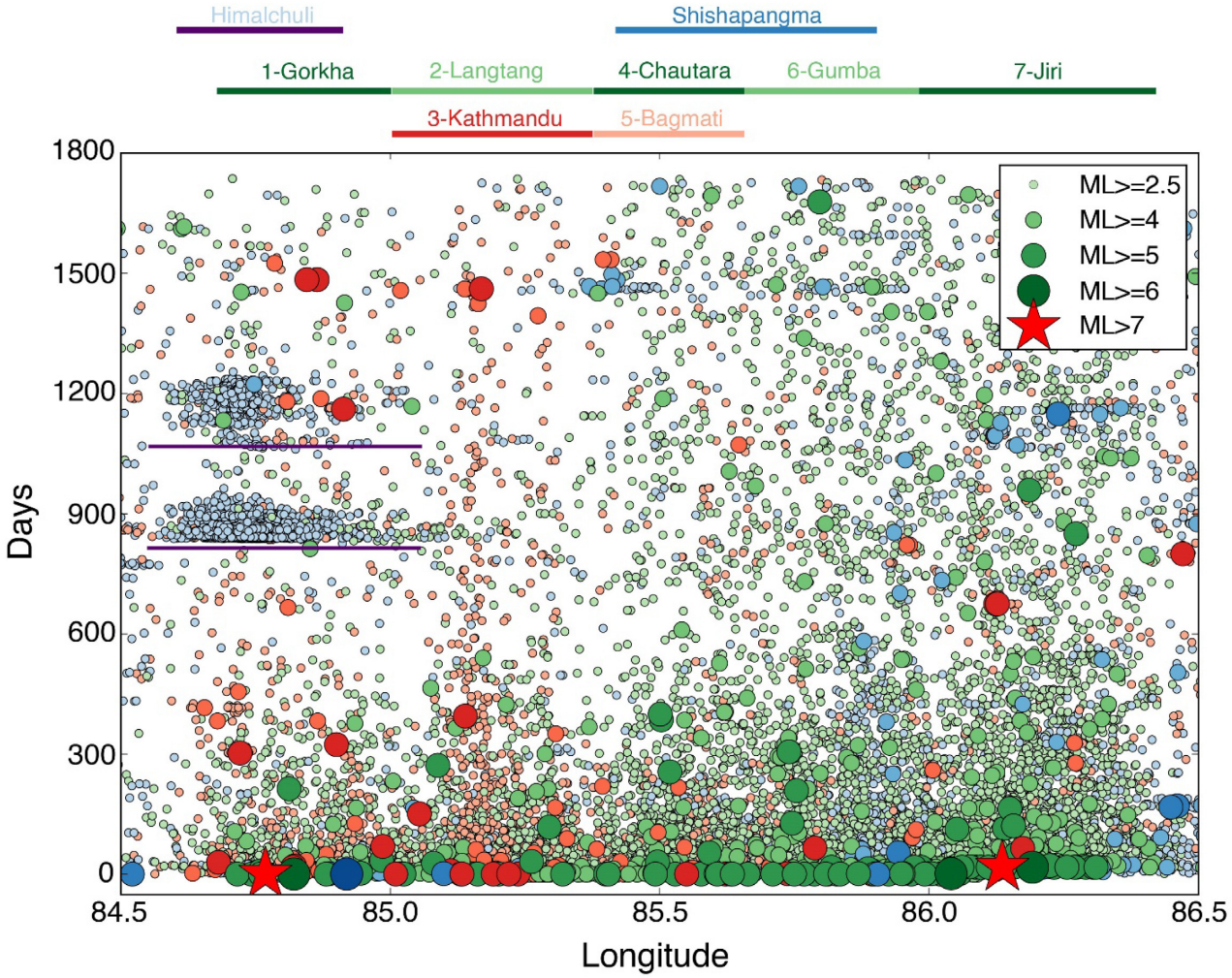

Figure 8. Time sequence of the earthquakes as a function of their longitudes. The events colour-coded in red and green are respectively located south and north from the main ruptured area. Blue events happened north of the interseismic mid-crustal cluster, under the High Himalayas and the southern Tibetan plateau. The extent of the zones delineated in Fig. 6 are represented at the top of the figure. The circles are colour-coded as a function of which zone they fall into—see the red/green and blue separators in Figs 4 and 7.

to other clusters described here, it does not follow the rupture at depth but may be related to the reactivation of a local structure (Baillard *et al*. 2017). Indeed, the seismicity there is parallel to the surface trace of the contact between the Lesser Himalayas and the Kathmandu klippe and is likely to fall within this shear zone at depth, given the dip of the structures. Further east, the seismicity of the mid-crustal clusters is spread over a wider area, about 25 km wide in Gumba zone and up to 40 km in Jiri, further East.

All these distinct zones are consistent with the segmentation of the seismicity along strike described by Baillard *et al.* (2017).

4.2 Time evolution of seismicity in each segment

The time-series of seismicity are overall similar in the various zones (Fig. 10 and Supporting Information Fig. S2), except for the case of the Himalchuli zone, where a swarm structure is observed (see Adhikari *et al.* 2021). Some differences are nevertheless observed among the various zones in the region of the aftershocks. For timescales shorter than a few months, the main difference is the initiation of the Kodari sequence to the east, which creates a burst of activity displacing the barycentre of all earthquakes (Supporting Information S7). While, during the first few hours and days, the peak activity tended to move from west to east, and back (see above), the barycentre position tended to be rather constant afterwards, and returned to its value after the decay of the Kodari sequence. Thus, overall, the average activity stabilized over time and remains similar after 5 yr, except for localized density peaks as developed below.

To the north (zones Gorkha, Langtang, Chautara, Gumba, Jiri; see Fig. 6), the aftershocks decay in a similar fashion, obeying the modified Omori Law followed by the complete catalogue of aftershocks (Supporting Information Text on the aftershock decay and the generalized Omori law), with an event rate remaining significantly higher in 2020 than during the preceding interseismic period. The southern Kathmandu and Bagmati zones are characterized by the absence of significant activity during more than 20 yr before (Supporting Information Fig. S8). The intense activity in these zones, widely felt in the densely populated Kathmandu Valley, played an important role in the perception of the Gorkha earthquake and its aftershocks and the spread of anxiety within the population. Despite its specificities (i.e. its shallower depths, location compared to the downdip end of the locked fault), the aftershocks in the Kathmandu zone follow the overall decay of the seismic activity (Fig. 10). In the northern zones,

Table 2. Properties of the aftershocks of the 2015 Gorkha earthquake for the period from 2015 April 25 to 2020 April 25—zones defined in Fig. 6

Zone	Range longitude latitude	Area (km^2)	n $M_L > 2.5$	Mean depth (km)	n $M_L > 5$	n $M_L > 6$	M_c	b	Maximum M_L	M_{co} (Nm)	ΣM (Nm)	$M^{eq}{}_w$
0 Himalchuli	84.6–84.9 28.35–28.6	815.14	6096	9.8 ± 0.1	0	0	2.9	3.7	4.1 18:50 25/04/2015		3.5×10^{16}	4.96
1 Gorkha	84.63–85.03 27.8–28.25	1964.60	1426	10.4 ± 0.1	21	3	2.5	0.81 ± 0.02	6.7 6:45 25/04/2015	9.84×10^{19}	1.28×10^{19}	6.67
1A	84.63–84.82 27.95–28.25	531.83	513	10.2 ± 0.4	8	1	2.5	0.76 ± 0.02	5.8 10:10 21/02/2016	2.46×10^{19}	7.65×10^{17}	5.86
1B	84.82–85.03 27.8–28.2	733.35	831	10.3 ± 0.2	10	1	2.5	0.82 ± 0.01	6.0 6:15 25/04/2015	4.62×10^{19}	1.88×10^{18}	6.12
2 Langtang	85.03–85.4 27.88–28.2	1292.09	1245	11.2 ± 0.1	8	0	2.5	0.99 ± 0.01	5.3 6:02 20/08/2015	1.40×10^{20}	2.68×10^{17}	5.55
2A	85.03–85.20 27.88–28.12	445.41	357	12.8 ± 0.5	2	0	2.3	1.03 ± 0.03	5.3 19:22 21/01/2016	6.69×10^{19}	6.83×10^{16}	5.16
2B	85.2–85.4 27.9–28.15	545.72	775	10.4 ± 0.2	5	0	2.4	0.98 ± 0.02	5.3 6:02 20/08/2015	6.32×10^{19}	1.76×10^{17}	5.43
3 Kathmandu	85.03–85.4 27.63–27.88	1012.11	1136	10.8 ± 0.1	9	0	2.0	0.91 ± 0.01	5.6 8:20 25/04/2015	8.96×10^{19}	5.58×10^{17}	5.76
4 Chautara	85.4–85.7 27.75–28.1	1147.08	2606	9.3 ± 0.1	15	0	2.1	0.93 ± 0.01	5.7 6:25 25/04/2015	1.61×10^{20}	1.18×10^{18}	5.98
5 Bagmati	85.4–85.7 27.49–27.75	854.51	412	8.5 ± 0.4	2	0	2.3	0.99 ± 0.01	5.8 8:55 25/04/2015	2.76×10^{19}	3.56×10^{17}	5.63
6 Gumba	85.7–85.9 27.6–28	874.98	2404	10.6 ± 0.1	17	0	2.2	0.91 ± 0.01	5.8 16:26 26/04/2015	3.77×10^{19}	1.5×10^{18}	6.05
7 Jiri	85.9–86.4 27.48–27.95	2572.25	5130	11.7 ± 0.1	39	3	2.3	0.88 ± 0.02	6.9 7:09 26/04/2015	1.13×10^{20}	2.78×10^{19}	6.90
7W	85.9–86 27.66–27.94	306.24	1080	11.9 ± 0.2	9	0	2.3	0.88 ± 0.01	5.5 7:26 26/04/2015	2.13×10^{19}	6.11×10^{17}	5.79
7C	86–86.2 27.62–27.9	612.71	2119	11.9 ± 0.1	18	3	2.3	0.78 ± 0.02	6.9 7:09 26/04/2015	3.17×10^{19}	2.63×10^{19}	6.88
7E	86.2–86.4 27.55–27.8	547.49	1146	11.4 ± 0.2	8	0	2.5	0.91 ± 0.01	5.7 7:10 12/05/2015	0	6.77×10^{17}	5.82
Aftershocks	Zones 1– 7	9717.63	14 362	10.7 ± 0.1	111	6	2.3	0.96 ± 0.01	6.9 7:09 26/04/2015	6.02×10^{20}	4.45×10^{19}	7.03

Table 3. Summary of parameters of the Omori law. The fit of Omori law corresponds to model 3 in Woessner *et al.* (2004). The parameters of the generalized Omori law by Shcherbakov *et al.* (2004) are calculated using the given value of c. The numerical values of the constants are then calculated. The value of parameter a, as defined in Hardebeck *et al.* (2019), is obtained from the calculated values of constants K_1.

$M_L >$	Fit of Omori law			Generalized Omori law			a
	p_1	c	k_1	c	K_1	k_1	
2.5	1.13 ± 0.01	4.45 ± 0.12	4244 ± 15	4.45	753	4515	−1.53
3	1.18 ± 0.01	2.33 ± 0.10	1897 ± 88	2.33	476	1313	−1.59
3.5	1.18 ± 0.01	0.91 ± 0.10	514 ± 36	1.4	262	393	−1.63

located above the MHT ramp (Fig. 6), the activity was permanent during the interseismic period. In the Gorkha zone (Supporting Information Fig. S8), the 2001 July 16 event, mentioned above, was the largest earthquake in the whole region. Another significant earthquake, with $M_L = 5.3$, had occurred in the same zone on 2011 November 11, with epicentre (28.186°N, 85.949°E), 17 km from the epicentre of the Gorkha earthquake. This is already a first hint towards the fact detailed below, that clusters of earthquakes, in the interseismic and post-seismic periods, tend to accumulate preferably near the same locations.

While larger earthquakes, with magnitude M_L larger than 5, were more frequent at the beginning of the crisis, an increase in activity is observed in the Jiri zone in 2017, while persisting activity and possibly a late increase is observed in the Gorkha, Gumba and

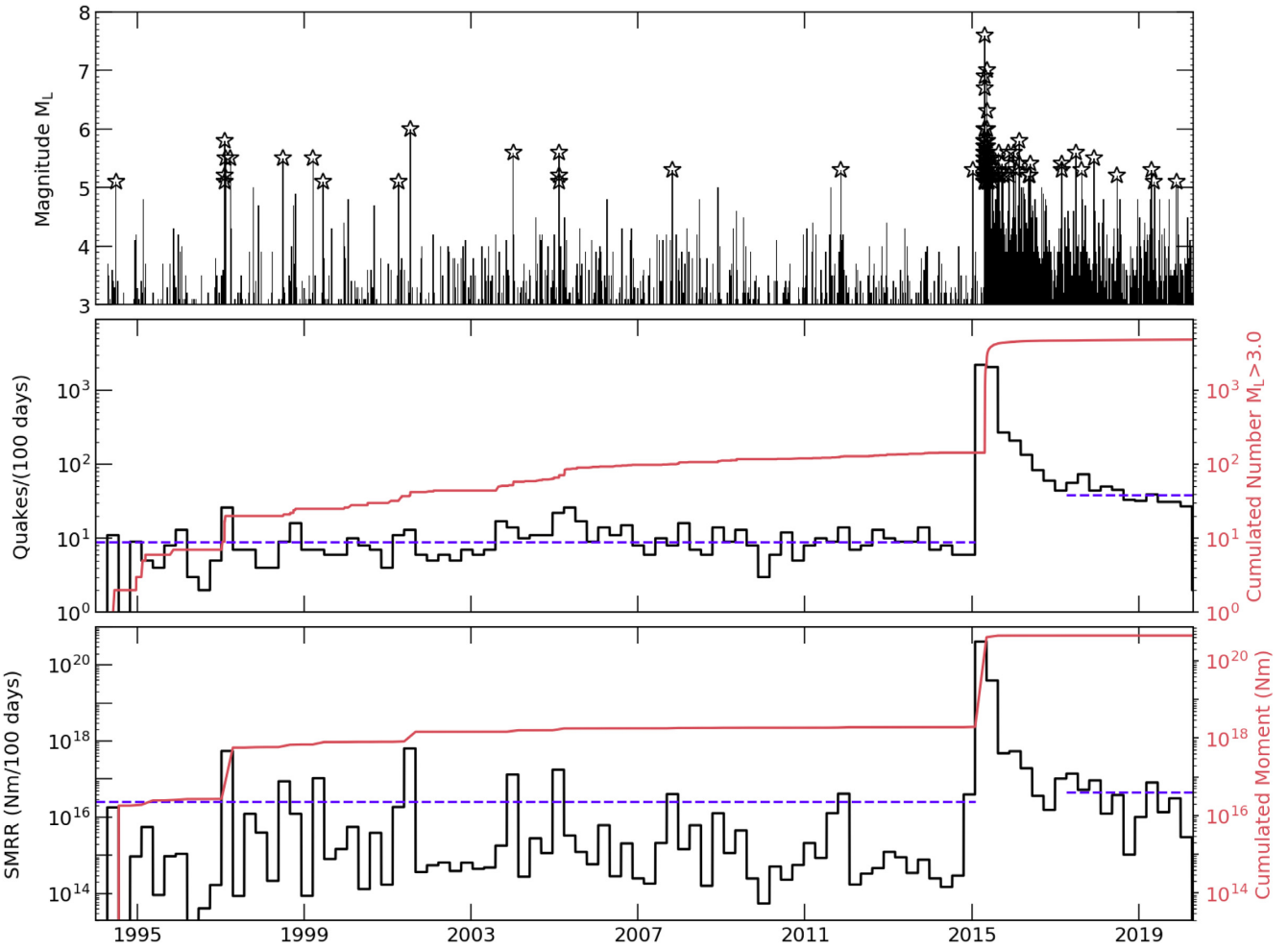

Figure 9. Time structure of the seismicity from 1994 to 2020 in the rupture zone of the Gorkha earthquake. (a) Earthquake magnitude distribution. Stars indicate earthquake with M_L larger than 5. (b) Rate of earthquakes (/100 d) and cumulated number of $M_L > 3.0$ (in grey). (c) Cumulated moment dissipated (in Nm). Horizontal lines in panels (b) and (c), covering a time interval, indicate the mean value during the considered interval.

Kathmandu zones. Recently, an M_L 5.9 earthquake occurred on 2020 September 16 in the Gumba zone, widely felt in Kathmandu.

4.3 Relations between aftershocks and tectonic structures

The aftershocks of the Gorkha earthquake were then confronted to the geological structures at depth. Indeed, the geometry of the tectonic structures at depth were locally extrapolated from surface geological observations, or imaged by geophysical techniques. In the region, the Main Himalayan Thrust remains principally imaged by the Receiver Function images generated after the Hi-Climb experiment (Nábelek *et al.* 2009; Duputel *et al.* 2016) complemented by seismic reflection imagery (Kurashimo *et al.* 2019) for the Kathmandu region, and after Hi-Mnt experiment in eastern Nepal (Schulte-Pelkum *et al.* 2005).

However, the position, dip and depth of the low-velocity zone imaged by the receiver function analysis from the Hi-Climb experiment are only marginally consistent with some of the geological cross-sections published in these areas (e.g. Schelling 1992; Pearson 2002; Khanal & Robinson 2013; Robinson & Martin 2014; Elliot *et al*. 2016 ; Hubbard *et al.* 2016; Whipple *et al*. 2016; Ghoshal *et al* . 2020). Indeed, the depth and dip of the MHT decollement differs significantly between the authors, from 10 to 20 km, and from 2° to 10°, with or without mid-crustal ramp(s). We projected the catalogue of earthquakes of the Kathmandu–Langtang (Fig. 5) on the balanced cross-section from Hubbard *et al.* (2016; Fig. 11). The seismicity projects mainly along the downdip end of the intermediate flat. The Kathmandu seismicity occurs in the vicinity of a secondary ramp which separates the upper and intermediate flats of a double-decked structure. The shape of the seismicity clusters at depth, at two distinct depths, corresponds well with the structure of the MHT despite the absolute depths of the events, which appear 5 km deeper than the structures.

We did the same with the Bagmati-Chautara region, projected on Hubbard *et al.* (2016), despite the significant distance to the geological cross-section and the lateral variations of the structures (Fig. 12).

The remaining cross-sections further west (Supporting Information Fig. S8) and east (Supporting Information Figs S9–S11) are respectively projected on Whipple *et al.* (2016), Hubbard *et al.* (2016) and Schelling (1992).

4.4 A persistent segmentation of the seismicity at seismic cycle scale

As previously mentioned, and illustrated in Figs 2 and 4, the seismicity shows along strike heterogeneities. More than the map of

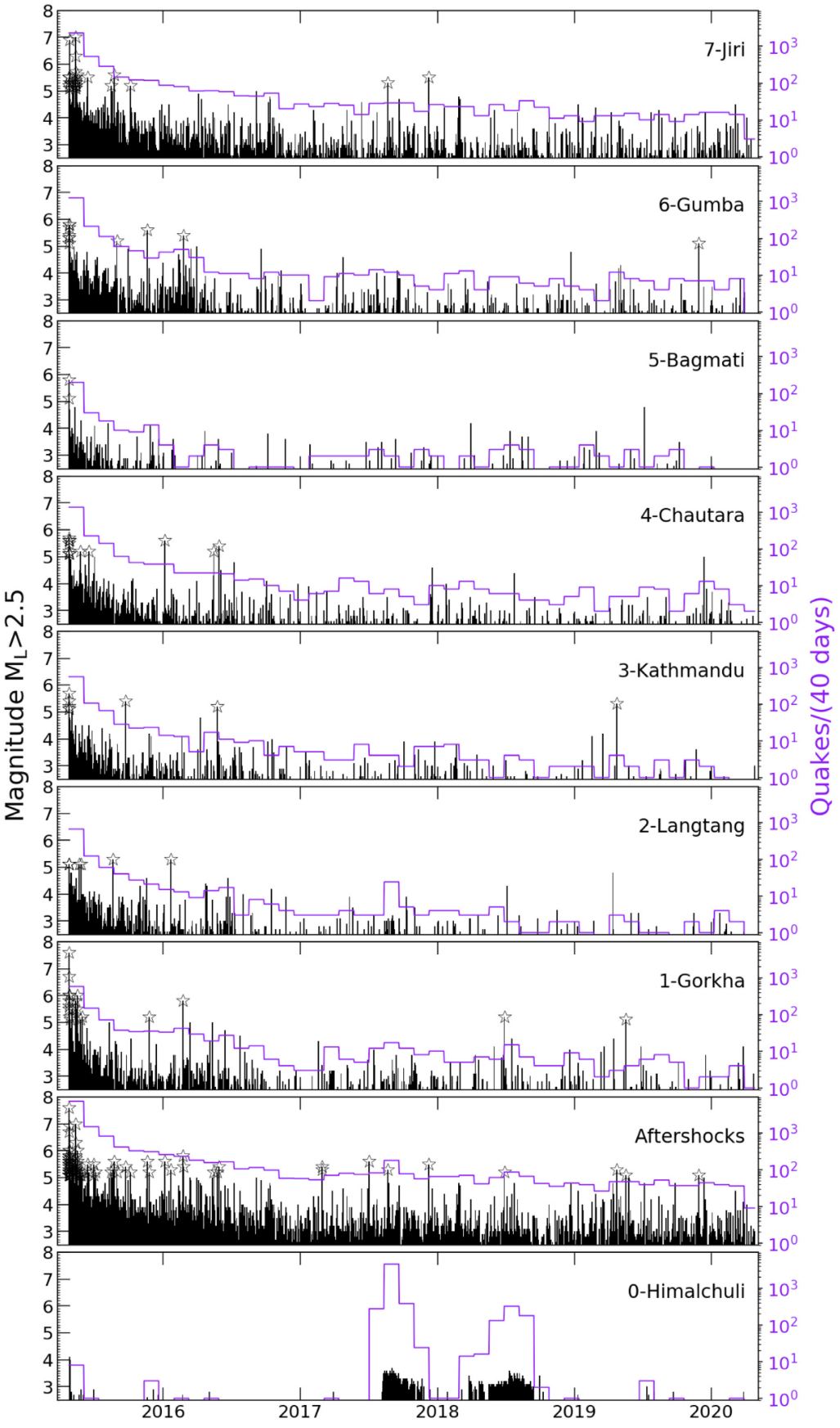

Figure 10. Time structure of the seismicity since the main shock in every zone (defined in Fig. 6). The histograms refer to the number of events per period of 40 d with the scale given to the right.

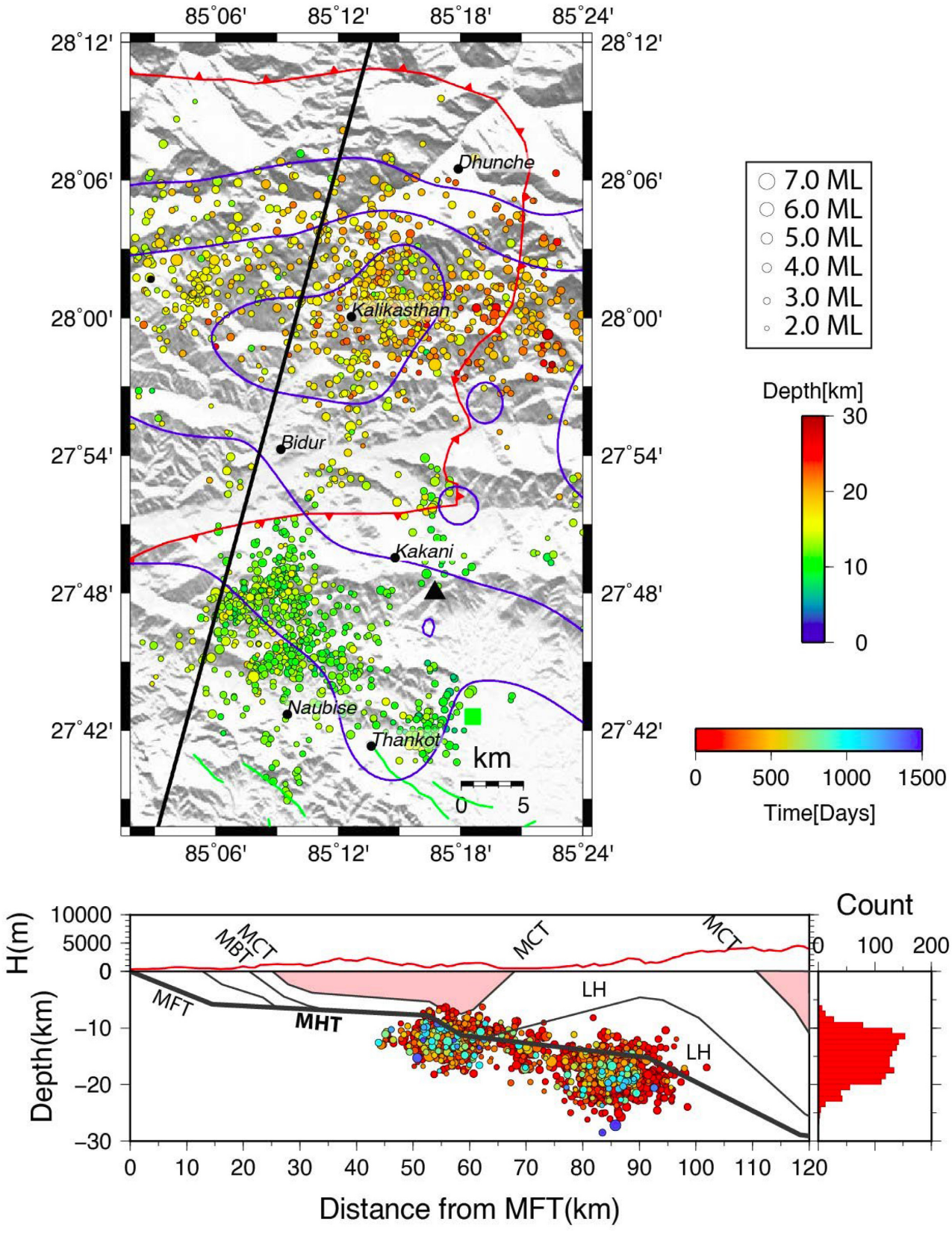

Figure 11. Seismicity map and cross-section of the Kathmandu–Langtang region. Epicentres from HypoDD relative relocation, after selecting high-quality events, documented by at least 10 phases (P + S). Phase and distance weighting from Hypo71. Balanced cross-section projected from Hubbard *et al.* (2016). The crystalline rocks of the High Himalaya and Kathmandu klippe are shown in pink.

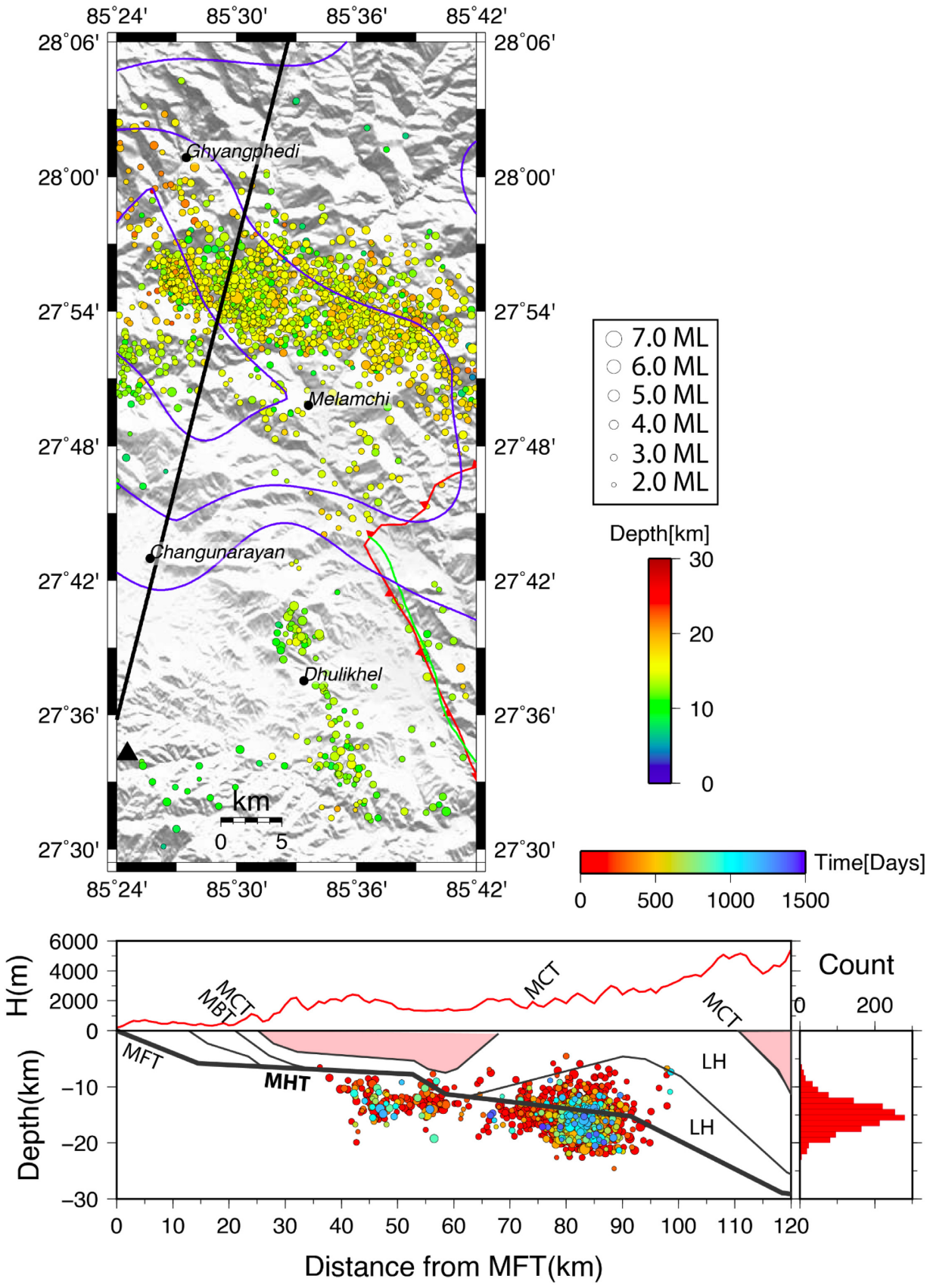

Figure 12. Seismicity map of the Chautara–Bagmati region. Epicentres from HypoDD relative relocation, after selecting high-quality events, documented by at least 10 phases (P + S). Phase and distance weighting from Hypo71. Balanced cross-section projected from Hubbard *et al.* (2016). The GHS geological domain is shown in pink.

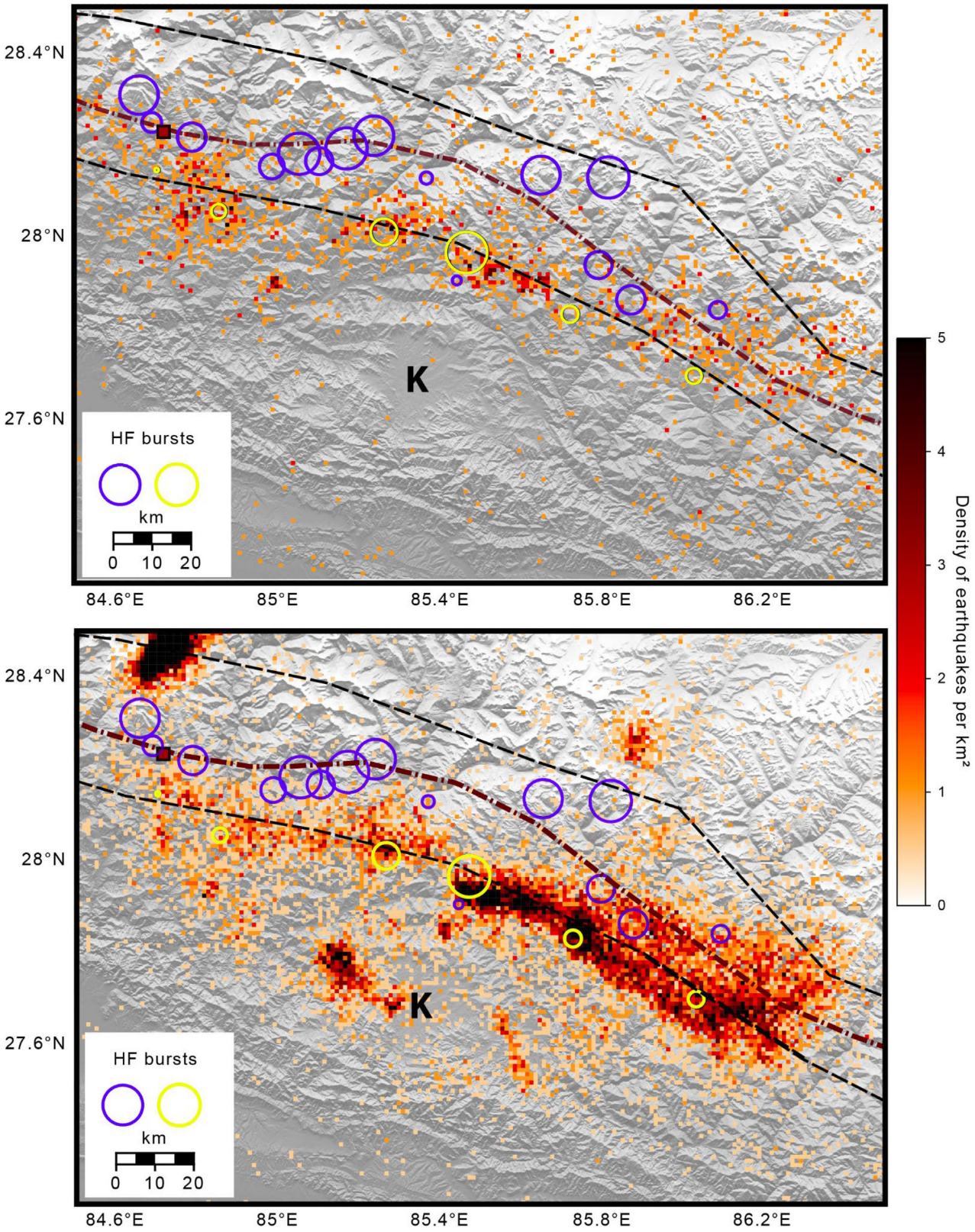

Figure 13. Confrontation between (a) the density of seismicity during the interseismic period (1994–2014) and (b) the density of aftershocks after the 2015 April 25 M_w 7.9 Gorkha earthquake. Density of earthquakes is computed as the log normalized of the number of events greater than M_L 2.5 per km^2. Brown dot-dashed line is the geologically inferred location of the base of the mid-crustal ramp (Hubbard *et al.* 2016). Black dashed lines correspond to the 95 per cent confidence range for the downdip extent of the coupling from Lindsey *et al*. (2018). Yellow circles are the high-frequency (0.5–4 Hz) peaks inferred from the backprojection of teleseismic *P* waves during the Gorkha rupture (Qin & Yao 2017). Blue circles are the high-frequency (1–4 Hz) peaks inferred from the backprojection of teleseismic *P* waves during the Gorkha rupture (Grandin *et al.* 2015). Size of circles depends on the normalized peak energy. Peaks locations depend on the relative location of the hypocentre. K, Kathmandu.

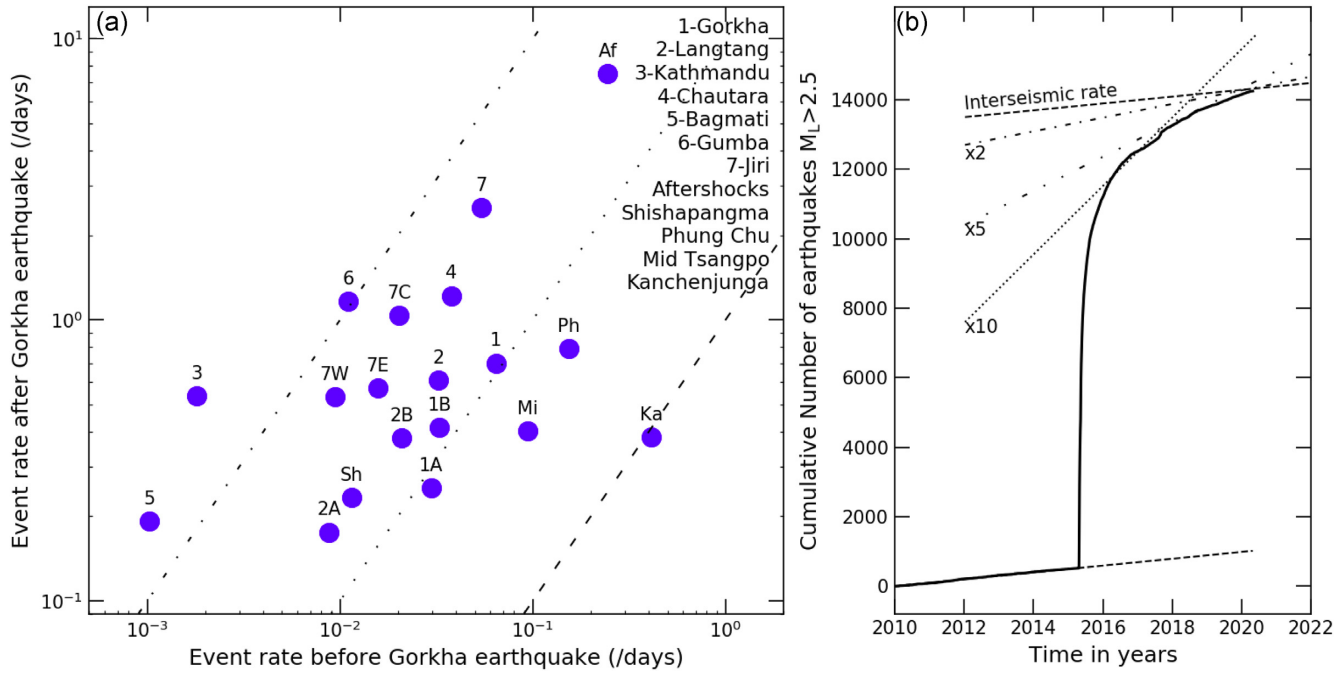

Figure 14. (a) Event rate before and after the Gorkha earthquake (in number of earthquakes with $M_L > 2.5$ d^{-1}). The numbers and letters refer to the zones and subzones listed on the right and are shown in Fig. 6. The dashed line refers to a ratio of 1, the dotted line to a ratio of 10 and the dash-dotted line to a ratio of 100. (b) Cumulated number of earthquakes from 2010 to 2020. The dashed lines refer to the interseismic rate. The dash-dotted, double dash-dotted and dotted lines respectively refer to a 2, a 5 and a 10 times rate. The rate of the seismicity in the trace of the Gorkha earthquake is still about 5 times larger than before the earthquake.

epicentres, the density distribution of the earthquakes computed as the log of the number of earthquakes above the completeness magnitude per km^2 highlights these seismic lateral variations. Both interseismic (Fig. 13a integrating 20 yr of seismicity) and post-seismic maps (Fig. 13b integrating 5 yr of aftershocks) show strong lateral variations along the down-dip extent of the coupling (southernmost dashed line on Fig. 13). Indeed, the seismic rate is high in the regions (a) between 84.7°E and 84.9°E, (b) between 85.2°E and 85.3°E, (c) between 85.5°E and 85.7°E and eastward (d) between 85.9°E and 86.2°E. The last two regions are 20-km-long stretches of seismicity oriented respectively N110° and N130° while (a) and (b) are more stocky.

Surprisingly, these maxima correspond to distinct features in the coseismic slip map determined from the joint inversion of geodetic and seismological data (Grandin *et al.* 2015): (a) at the onset; (b and c) at the peaks of the coseismic slip. The width and orientation of (c) coincides with a northward excursion of the coseismic slip, while (d) underlines the extent of the patch ruptured during the May 12th earthquake.

These maxima also correspond to some peaks of high-frequency, coseismic bursts (yellow on Fig. 13) determined from the back-projection of teleseismic *P*-waves generated during the Gorkha earthquake. These bursts were estimated by Qin & Yao (2017) as the summed power of multiple arrays filtered between 0.5–4 Hz and cross-correlated. These high frequency bursts fall at short distances from the beginning or end of (a), (b) and (c) (Figs 13a and b).

Alternative estimates of the high frequency bursts exist (e.g. Avouac *et al.* 2015; Grandin *et al.* 2015) and were determined with different arrays, methods and frequency bands, giving different results. For instance, the high frequency emissions characterized by Grandin *et al.* (2015) were filtered in a higher frequency band from 1 to 4 Hz and represented array by array filtered between 1.0 and 4.0 Hz, cross-correlated and weighted by semblance. They seem to underline a deeper and farther in the north process along the Main Himalayan Thrust, falling at short distances from the geologically inferred location of the base of the mid-crustal ramp of Hubbard *et al.* (2016).

Overall, the heterogeneities in the seismicity along the downdip extent of the coupling appear persistent during the interseismic, co-seismic and post-seismic phases of the seismic cycles. They fall at short distances from heterogeneities in the coseismic slip and high frequency seismic bursts generated during the rupture. All these heterogeneities participate in the segmentation of the seismicity along strike, a segmentation possibly controlled by geological structural complexities of the Main Himalayan Thrust fault.

We suggest that these clusters revealed, during the interseismic period, the seismo-geological segmentation which influences both the coseismic rupture and the post-seismic relaxation.

Zones of peak density in events rate in Fig. 13, and transitions in Supporting Information Fig. S12, correspond also to the limits of the zones and subzones defined in Fig. 8. Lateral segmentation of the MHT thus should also appear when comparing the interseismic event rate with the mean post-seismic event rate per zones (Fig. 14, Supporting Information Fig. S13). In this figure, zones with the same post-seismic/interseismic amplification factor are located on the line parallel to the dashed diagonal line. The zones most affected by the Gorkha earthquake are the Gumba zone to the North, and, obviously, the Kathmandu and Bagmati zones where activity was rare during the interseismic period. In addition, when subzones are considered, they are located on a line, to which the complete zone also belongs. This is specially the case for points 2, 2A, 2B on the one hand and points 7, 7C, 7 W, 7E on the other hand. This implies

that the local transitions suggested in Fig. 13 define the boundaries of approximately homogeneous segments. The differences between the segments seem approximately stable with time during the post-seismic period.

5 CONCLUSION

The 50 000 + earthquakes located by the NEMRC network during the 5 yr that followed the large M_w 7.9 Gorkha Nepal earthquake reveal a temporal decay of the aftershock rates that appears following a generalized Omori law (Supporting Information Fig. S3).

The empirical relation tied by the data available at the end of 2020 suggests that the rate of the aftershocks with a magnitude above $M_c = 2.5$ will remain higher than the seismicity rate obtained before 2015, during a period of approximately 20 yr following the main shock. This result is consistent with the projections of the deep afterslip relaxation monitored by geodesy. The afterslip rate projections remain, on average, larger than 10 per cent of the slip rate on the fault—probably influencing the seismicity related with the stress build up—between 10 and 20 yr following the earthquake (Gualandi *et al.* 2017). This suggests that the rate of earthquakes will probably take slightly more than another decade to decrease down to pre-earthquake values, in the event that no new strong earthquake occurs. This result necessitates further confirmation using ETAS and physics based models, out of the scope of the present article.

In addition, the catalogue of earthquakes depicts a persistent, heterogeneous distribution of the aftershocks along strike, the fault segments ruptured during the main shock and the M_w 7.2 Kodari earthquake.

The main conclusion drawn from the study of these seismicity heterogeneities is that the segmentation of the aftershocks along the downdip end of the rupture has some similarities with the segmentation of the seismicity that occurred during the decades before the earthquake. In addition, the high frequency bursts that radiated along the downdip end of the rupture as well as the coseismic slip happening at depth on the Main Himalayan Thrust appear to reveal a segmentation of the coseismic rupture. This is consistent with the heterogeneity which develops at the scales of the interseismic and post-seismic periods, similarly to what was found along subduction zones (e.g. Soto-Cordero *et al.* 2020).

We therefore suggest that some along-strike heterogeneities in the seismicity are persistent over the whole seismic cycle and might therefore be related to mid-crustal frictional and/or structural heterogeneities.

ACKNOWLEDGMENTS

This work is part of the first author's doctoral thesis. We thank Nepal DMG as well as CEA/DASE, France for facilitating this work during the crisis that followed the Gorkha earthquake. The authors are most grateful to Mr Sarbajit Prasad Mahato, Dr Soma Nath Sapkota, Mr Rajendra Prasad Khanal and Mr Ram Prasad Ghimire, successive directors of DMG during the experience. We thank all the staff of the DMG and DASE who have contributed to the maintenance of the network. Mr Kamal Kafle and Mr Arjun Bhandari are also thanked for their involvement in the seismic bulletins processing. We thank the RSC team for his involvement in the processing of the aftershocks of the Gorkha earthquake also recorded from the distance at the RSC network. Finally, we acknowledge the editor Margarita Segou and two anonymous reviewers that provided comments that helped improve a previous version of this paper.

DATA AVAILABILITY

Data are available on request.

REFERENCES

Ader, T. *et al.* 2012. Convergence rate across the Nepal Himalaya and interseismic coupling on the Main Himalayan Thrust: Implications for seismic hazard, *J. geophys. Res.: Solid Earth,* **117**(B4).

Adhikari, L. B. *et al.*, 2015. The aftershock sequence of the 2015 April 25 Gorkha–Nepal earthquake, *Geophys. J. Int.,* **203**(3), 2119–2124

Adhikari, L.B. *et al.*, 2021. Orogenic collapse and stress adjustments revealed by an intense seismic swarm following the 2015 Gorkha earthquake in Nepal, *Front. Earth Sci.,* **9,** doi:10.3389/feart.2021.659937.

Adhikari, L.B., 2021. Seismicity associated with the April 25, 2015 Gorkha earthquake in Nepal: probing the Himalayan seismic cycle, *PhD thesis,* University of Paris, Institut de Physique du globe de Paris, France.

Avouac, J. P., Bollinger, L., Lavé, J., Cattin, R. & Flouzat, M., 2001. Le cycle sismique en Himalaya, *C. R. Acad. Sci., Paris II,* **333**(9), 513–529.

Avouac, J. P., Meng, L., Wei, S., Wang, T. & Ampuero, J. P., 2015. Lower edge of locked Main Himalayan Thrust unzipped by the 2015 Gorkha earthquake, *Nat. Geosci.,* **8**(9), 708–711.

Bai, L., Klemperer, S. L., Mori, J., Karplus, M. S., Ding, L., Liu, H. & Dhakal, S., 2019. Lateral variation of the Main Himalayan Thrust controls the rupture length of the 2015 Gorkha earthquake in Nepal, *Sci. Adv.,* **5**(6), eaav0723.

Bai, L., Liu, H., Ritsema, J., Mori, J., Zhang, T., Ishikawa, Y. & Li, G., 2016. Faulting structure above the Main Himalayan Thrust as shown by relocated aftershocks of the 2015 Mw7. 8 Gorkha, Nepal, earthquake, *Geophys. Res. Lett.,* **43**(2), 637–642.

Baillard, C., Lyon-Caen, H., Bollinger, L., Rietbrock, A., Letort, J. & Adhikari, L. B., 2017. Automatic analysis of the Gorkha earthquake aftershock sequence: evidences of structurally segmented seismicity, *Geophys. J. Int.,* **209**(2), 1111–1125.

Bollinger, L., Avouac, J.P., Cattin, R. & Pandey, M.R., 2004. Stress build up in the Himalaya, *J. geophys. Res.,* **109,** B11405.

Bollinger, L., Perrier, F., Avouac, J. P., Sapkota, S., Gautam, U. T. D. R. & Tiwari, D. R., 2007. Seasonal modulation of seismicity in the Himalaya of Nepal, *Geophys. Res. Lett.,* **34**(8), doi:10.1029/2006GL029192.

Burtin, A., Bollinger, L., Cattin, R., Vergne, J. & Nábělek, J.L., 2009. Spatiotemporal sequence of Himalayan debris flow from analysis of high-frequency seismic noise, *J. geophys. Res.,* **114,** doi:10.1029/2008JF001198.

Burtin, A., Bollinger, L., Vergne, J., Cattin, R. & Nábělek, J.L., 2008. Spectral analysis of seismic noise induced by rivers: a new tool to monitor spatiotemporal changes in stream hydrodynamics, *J. geophys. Res.,* **113,** B05301.

Cattin, R. & Avouac, J. P., 2000. Modeling mountain building and the seismic cycle in the Himalaya of Nepal, *J. geophys. Res.: Solid Earth,* **105**(B6),13389–13407.

Denolle, M. A., Fan, W. & Shearer, P. M., 2015. Dynamics of the 2015 M7. 8 Nepal earthquake, *Geophys. Res. Lett.,* **42**(18), 7467–7475.

Duputel, Z., Vergne, J., Rivera, L., Wittlinger, G., Farra, V. & Hetényi, G., 2016. The 2015 Gorkha earthquake: a large event illuminating the Main Himalayan Thrust fault, *Geophys. Res. Lett.,* **43,** 2517–2525.

Duverger, C., Mazet-Roux, G., Bollinger, L., Guilhem Trilla, A., Vallage, A., Hernandez, B. & Cansi, Y., 2021. A decade of seismicity in metropolitan France (2010–2019): the CEA/LDG methodologies and observations, *Bull. Soc. Geol. Fr.,* **192**(1), 25.

Elliott, J. R., Jolivet, R., González, P. J., Avouac, J. P., Hollingsworth, J., Searle, M. P. & Stevens, V. L., 2016. Himalayan megathrust geometry and relation to topography revealed by the Gorkha earthquake, *Nat. Geosci.,* **9**(2), 174–180.

Galetzka, J. *et al.*, 2015. Slip pulse and resonance of the Kathmandu basin during the 2015 Gorkha earthquake, Nepal, *Science,* **349**(6252), 1091–1095.

Geiger, H., 1910. The scattering of α-particles by matter, *Proceedings of the Royal Society of London. Series A, Containing Papers of a Mathematical and Physical Character,* **83**(565), 492–504.

Ghoshal, S., McQuarrie, N., Robinson, D. M., Adhikari, D. P., Morgan, L. E. & Ehlers, T. A., 2020. Constraining central Himalayan (Nepal) fault geometry through integrated thermochronology and thermokinematic modeling, *Tectonics,* **39**(9), e2020TC006399

Grandin, R., Vallée, M., Satriano, C., Lacassin, R., Klinger, Y., Simoes, M. & Bollinger, L., 2015. Rupture process of the Mw = 7.9 2015 Gorkha earthquake (Nepal): insights into Himalayan megathrust segmentation, *Geophys. Res. Lett.,* **42**(20), 8373–8382.

Gualandi, A. *et al.*, 2017. Pre- and post-seismic deformation related to the 2015, Mw7.8 Gorkha earthquake, Nepal, *Tectonophysics,* **714–715,** 90–106

Hardebeck, J. L., Llenos, A. L., Michael, A. J., Page, M. T. & Van Der Elst, N., 2019. Updated California aftershock parameters, *Seismol. Res. Lett.,* **90**(1),262–270.

Holtkamp, S. & Brudzinski, M.R., 2014. Megathrust earthquake swarms indicate frictional changes which delimit large earthquake ruptures, Earth planet, *Sci. Lett.,* **390,** 234–243.

Hong, S. & Liu, M., 2021. Postseismic deformation and afterslip evolution of the 2015 Gorkha earthquake constrained by InSAR and GPS observations, *J. geophys. Res.,* **126**(7), e2020JB020230.

Hoste-Colomer, R. *et al.*, 2018. Lateral variations of the mid-crustal seismicity in western Nepal: seismotectonic implications, *Earth planet. Sci. Lett.,* **504,** 115–125.

Hoste-Colomer, R., Bollinger, L., Lyon-Caen, H., Burtin, A. & Adhikari, L.B., 2017. Lateral structure variations and transient swarm revealed by seismicity along the Main Himalayan Thrust north of Kathmandu, *Tectonophysics,* **714–715,** 107–116.

Hubbard, J., Almeida, R., Foster, A., Sapkota, S. N., Bürgi, P. & Tapponnier, P., 2016. Structural segmentation controlled the 2015 Mw 7.8 Gorkha earthquake rupture in Nepal, *Geology,* **44**(8), 639–642.

Jouanne, F., Gajurel, A., Mugnier, J. L., Bollinger, L., Adhikari, L. B., Koirala, B. & Huyghe, P., 2019. Postseismic deformation following the April 25, 2015 Gorkha earthquake (Nepal): afterslip versus viscous relaxation, *J. Asian Earth Sci.,* **176,** 105–119.

Karplus, M. S., Pant, M., Sapkota, S. N., Nábělek, J., Velasco, A. A., Adhikari, L. B. & Braunmiller, J., 2020. A rapid response network to record aftershocks of the 2015 M 7.8 Gorkha earthquake in Nepal, *Seismol. Res. Lett.,* **91,** 2399–2408.

Khanal, S. & Robinson, D. M., 2013. Upper crustal shortening and forward modeling of the Himalayan thrust belt along the Budhi-Gandaki River, central Nepal, *Int. J. Earth Sci.,* **102**(7), 1871–1891

Kobayashi, T., Morishita, Y. & Yarai, H., 2015. Detailed crustal deformation and fault rupture of the 2015 Gorkha earthquake, Nepal, revealed from ScanSAR-based interferograms of ALOS-2, *Earth Planets Space,* **67**(1), 1–13

Kurashimo, E., Sato, H., Sakai, S. I., Hirata, N., Gajurel, A. P., Adhikari, D. P. & Upreti, B. N., 2019. The 2015 Gorkha earthquake: earthquake reflection imaging of the source fault and connecting seismic structure with fault slip behavior, *Geophys. Res. Lett.,* **46**(6), 3206–3215

Laporte, M. *et al.*, 2021. Seismicity in far western Nepal reveals flats and ramps along the Main Himalayan Thrust, *Geophys. J. Int.,* **226**(3), 1747–1763.

Lay, T., Ye, L., Koper, K. D. & Kanamori, H., 2017. Assessment of teleseismically-determined source parameters for the April 25, 2015 MW 7.9 Gorkha, Nepal earthquake and the May 12, 2015 MW 7.2 aftershock, *Tectonophysics,* **714,** 4–20.

Lee, W. H. K. & Lahr, J., 1972. HYPO71: A computer program for determining hypocenter, magnitude, and first motion pattern of local earthquakes, *US Department of the Interior, Geological Survey, National Center for Earthquake Research*.

Letort, J., Bollinger, L., Lyon-Caen, H., Guilhem, A., Cano, Y., Baillard, C. & Adhikari, L. B., 2016. Teleseismic depth estimation of the 2015 Gorkha– Nepal aftershocks, *Geophys. J. Int.,* **207**(3), 1584–1595

Li, L., Yao, D., Meng, X., Peng, Z. & Wang, B., 2017. Increasing seismicity in Southern Tibet following the 2015 Mw 7.8 Gorkha, Nepal earthquake, *Tectonophysics,* **714–715,** 62–70

Lindsey, E. O. *et al.* 2018. Structural control on downdip locking extent of the Himalayan megathrust, *J. geophys. Res.: Solid Earth,* **123**(6), 5265–5278.

Lindsey, E. O., Natsuaki, R., Xu, X., Shimada, M., Hashimoto, M., Melgar, D. & Sandwell, D. T., 2015. Line-of-sight displacement from ALOS-2 interferometry: Mw 7.8 Gorkha earthquake and Mw 7.3 aftershock, *Geophys. Res. Lett.,* **42**(16), 6655–6661

Liu-Zeng, J., Zhang, Z., Rollins, C., Gualandi, A., Avouac, J. P., Shi, H. & Li, Z., 2020. Postseismic deformation following the 2015 Mw7. 8 Gorkha (Nepal) earthquake: new GPS data, kinematic and dynamic models, and the roles of afterslip and viscoelastic relaxation, *J. geophys. Res.,* **125**(9), e2020JB019852.

Mencin, D., Bendick, R., Upreti, B. N., Adhikari, D. P., Gajurel, A. P., Bhattarai, R. R. & Knappe, E., 2016. Himalayan strain reservoir inferred from limited afterslip following the Gorkha earthquake, *Nat. Geosci.,* **9**(7), 533–537

Mendoza, M. M., Ghosh, A., Karplus, M. S., Klemperer, S. L., Sapkota, S. N., Adhikari, L. B. & Velasco, A., 2019. Duplex in the Main Himalayan Thrust illuminated by aftershocks of the 2015 Mw 7.8 Gorkha earthquake, *Nature Geoscience,* **12**(12), 1018–1022.

Monsalve, G., Sheehan, A., Schulte-Pelkum, V., Rajaure, S., Pandey, M. R. & Wu, F., 2006. Seismicity and one-dimensional velocity structure of the Himalayan collision zone: earthquakes in the crust and upper mantle, *J. geophys. Res.,* **111**(B10301).1–19.

Nábelek, J. *et al.*, 2009. Underplating in the Himalaya-Tibet collision zone revealed by the Hi-CLIMB experiment, *Science,* **325,** 1371–1374.

Pandey, M. R., Tandukar, R. P., Avouac, J. P., Vergne, J. & Heritier, T., 1999. Seismotectonics of the Nepal Himalaya from a local seismic network, *J. Asian Earth Sci,* **17**(5-6), 703–712.

Pandey, M. R., Tandukar, R. P., Avouac, J. P., Lave, J. & Massot, J. P., 1995. Interseismic strain accumulation on the Himalayan crustal ramp (Nepal), *Geophys. Res. Lett.,* **22**(7), 751–754

Pearson, O. N., 2002. Structural evolution of the central Nepal fold-thrust belt and regional tectonic and structural significance of the Ramgarh thrust, *PhD dissertation*, 230pp., Department of Geosciences, University of Arizona, Tucson, AZ.

Qin, W. & Yao, H., 2017. Characteristics of subevents and three-stage rupture processes of the 2015 Mw 7.8 Gorkha Nepal earthquake from multiple-array back projection, *J. Asian Earth Sci.,* **133,** 72–79

Qiu, Q., Hill, E. M., Barbot, S., Hubbard, J., Feng, W., Lindsey, E. O. & Tapponnier, P., 2016. The mechanism of partial rupture of a locked megathrust: the role of fault morphology, *Geology,* **44**(10), 875–878

Robinson, D. M. & Martin, A. J., 2014. Reconstructing the Greater Indian margin: a balanced cross section in central Nepal focusing on the Lesser Himalayan duplex, *Tectonics,* **33**(11), 2143–2168

Ross, Z.E., Cochran, E.S., Trugman, D.T. & Smith, J.D., 2020 3D fault architecture controls the dynamism of earthquake swarms, *Science,* **368**(6497), 1357–1361.

Sapkota, S. N., Bollinger, L. & Perrier, F., 2016. Fatality rates of the M w∼ 8.2, 1934, Bihar–Nepal earthquake and comparison with the April 2015 Gorkha earthquake, *Earth, Planets and Space,* **68**(1), 1–9.

Sapkota, S. N., Bollinger, L., Klinger, Y., Tapponnier, P., Gaudemer, Y. & Tiwari, D., 2013. Primary surface ruptures of the great Himalayan earthquakes in 1934 and 1255, *Nature Geoscience,* **6**(1), 71–76.

Schelling, D., 1992. The tectonostratigraphy and structure of the eastern Nepal Himalaya, *Tectonics,* **11**(5), 925–943

Schulte-Pelkum, V., Monsalve, G., Sheehan, A., Pandey, M. R., Sapkota, S., Bilham, R. & Wu, F., 2005. Imaging the Indian subcontinent beneath the Himalaya, *Nature,* **435**(7046), 1222–1225

Segou, M. & Parsons, T., 2016. Prospective earthquake forecasts at the Himalayan Front after the 25 April 2015 M 7.8 Gorkha mainshock, *Seismol. Res. Lett.,* **87**(4), 816–825.

Shcherbakov, R., Turcotte, C.L. & Rundle, J.B., 2004. A generalized Omori's law for earthquake aftershock decay, *Geophys. Res. Lett.,* **31,** LL11613.

Soto-Cordero, L., Meltzer, A., Bergman, E., Hoskins, M., Stachnik, J. C., Agurto-Detzel, H. & Ruiz, M., 2020. Structural control on megathrust

rupture and slip behavior: insights from the 2016 Mw 7.8 Pedernales Ecuador Earthquake, *J. geophys. Res.,* **125**(2), e2019JB018001.

Sreejith, K. M., Sunil, P. S., Agrawal, R., Saji, A. P., Ramesh, D. S. & Rajawat, A. S., 2016. Coseismic and early postseismic deformation due to the 25 April 2015, Mw 7.8 Gorkha, Nepal, earthquake from InSAR and GPS measurements, *Geophys. Res. Lett.,* **43**(7), 3160–3168.

Waldhauser, F. & Ellsworth, W. L., 2000. A double-difference earthquake location algorithm: method and application to the northern Hayward fault, California, *Bull. seism. Soc. Am.,* **90**(6), 1353–1368.

Wang, X., Wei, S. & Wu, W., 2017. Double-ramp on the Main Himalayan Thrust revealed by broadband waveform modeling of the 2015 Gorkha earthquake sequence, *Earth planet. Sci. Lett.,* **473,** 83–93.

Whipple, K. X., Shirzaei, M., Hodges, K. V. & Ramon Arrowsmith, J., 2016. Active shortening within the Himalayan orogenic wedge implied by the 2015 Gorkha earthquake, *Nature Geoscience,* **9**(9), 711–716.

Woessner, J., Hauksson, E., Wiemer, S. & Neukomm, S., 2004. The 1997 Kagoshima (Japan) earthquake doublet: a quantitative analysis of aftershock rate changes, *Geophys. Res. Lett.,* **31,** L03605.

Woessner, J. & Wiemer, S., 2005. Assessing the quality of earthquake catalogues: estimating the magnitude of completeness and its uncertainty, *Bull. seism. Soc. Am.,* **95**(2), 684–698.

Yamada, M., Kandel, T., Tamaribuchi, K. & Ghosh, A., 2020. 3D Fault Structure Inferred from a Refined Aftershock Catalogue for the 2015 Gorkha earthquake in Nepal, *Bull. seism. Soc. Am.,* **110**(1), 26–37.

Zhao, B., Bürgmann, R., Wang, D., Tan, K., Du, R. & Zhang, R., 2017. Dominant controls of downdip afterslip and viscous relaxation on the postseismic displacements following the Mw7. 9 Gorkha, Nepal, earthquake, *J. geophys. Res.,* **122**(10), 8376–8401

SUPPORTING INFORMATION

Supplementary data are available at *GJI* online.

Figure S1 Distributions, for each of the seven zones in the aftershock domain (Fig. 6), of the major axis of the epicentre uncertainty ellipse (a), of the Primary Azimuthal Gap (b) and of the P (blue) and S phases (orange) picked in each seismic station of the NEMRC network.

Figure S2. GPS (red and blue) and aftershock rate time-series (black—expressed in events per period of 40 d) in central and eastern regions affected by the rupture. Zones are defined in Fig. 6. The location of the GPS stations CHLM (28°12′25.2″, 85°18′50.4″) and JIR2 (at JIRN, 27°39′25.2″N 86°11′13.2″) is shown in Fig. 7. The horizontal post-seismic displacement, referenced to 0 at the time of the Gorkha earthquake, is calculated subtracting the trend from a station outside the rupture zone (DNSG, 83°45′47″, 28°20′42″). All the data from the GPS stations can be found at http://geodesy.unr.edu/.

Figure S3. Seismicity rate (in number of events per day) versus time since main shock for three minimum local magnitude values. The curves correspond to the generalized Omori law (see the text) with the parameter values given in Table 3.

Figure S4. Time sequence of the earthquakes (in logarithmic scale from the time of the main shock of 2015 April 25, shown as the red star) as a function of their longitudes. The events colour coded in red and green are respectively located south and north from the main ruptured area. Blue events happened North of the interseismic mid-crustal cluster, under the High Himalayas and the southern Tibetan plateau.

Figure S5. Time sequence of the earthquakes for the first hours (in minutes) from the time of the main shock of 2015 April 25 as a function of their longitudes. The events colour coded in red and green are respectively located south and north of the main ruptured area. Blue events happened north of the interseismic mid-crustal cluster, under the High Himalayas and the southern Tibetan plateau.

Figure S6. Scaling properties of the aftershocks of the Gorkha earthquake. Two event rate ratios with different minimum magnitude values are shown.

Figure S7. Position of the barycentre of the aftershocks of the Gorkha earthquakes (earthquakes in zones 1–7 in Fig. 6), for three different minimum magnitude values. The purple and orange dashed lines show the position of the Gorkha and Kodari earthquakes, respectively.

Figure S8. Earthquake magnitudes (left scale) and event rate per period of 100 d (right scale) in the zones shown in Fig. 6 as a function of time since the beginning of the operation of the NSC network, for local magnitude M_L larger than 3. Aftershocks correspond to zones 1– 7.

Figure S9. Seismicity map and cross-section of the Gorkha region. Epicentres from HypoDD relative relocation, after selecting high quality events, documented by at least 10 phases (P + S). Phase and distance weighting from Hypo71. Balanced cross-sections from Whipple *et al*. (2016) and Elliot *et al*. (2016). The crystalline of the High Himalayas and Kathmandu klippe are shown in pink.

Figure S10. Seismicity map and cross-section of the Gumba region. Epicentres from HypoDD relative relocation, after selecting high quality events, documented by at least 10 phases (P + S). Phase and distance weighting from Hypo71. Balanced cross-section from Hubbard *et al.* (2016). The GHS geological domain is shown in pink.

Figure S11. Seismicity map and cross-section of the Jiri region. Epicentres from HypoDD relative relocation, after selecting high quality events, documented by at least 10 phases (P + S). Phase and distance weighting from Hypo71. Balanced cross-section from Schelling (1992). The GHS geological domain is shown in pink.

Figure S12. Profiles of the number of earthquakes with magnitude M_L larger than 2.5 (a) and cumulated moment (b) versus the distance projected onto the base of the MHT ramp (Hubbard *et al.* 2016). The blue lines refer to the interseismic period (1994–2015) and the red line to the post-seismic period (2015 April 25 to 2020 April 25).

Figure S13. Normalized Cumulated Moment (NMC) before (from 1994 to 2015) and after (from 2015 April 25 to 2020 April 25) the Gorkha earthquake (earthquakes with minimum local magnitude $M_L > 2.5$). The Cumulated Moment is normalized to the total number of days in the considered time period. The numbers and letters refer to the zones and subzones listed on the right and are shown in Figs 1(b) and 6.

Figure S14. Uncertainties Histograms in location and depth from HypoDD for each zone.

Table S1. Properties of the seismicity for the period from 1994 January 1 to 2015 April 24 in the zones defined on Fig. 6. For the earthquake rates, given for three M_L minimum magnitude, two time periods are considered: 1994 January 1 to 2004 December 31 (top number) and 2005 January 1 to 2015 April 24 (below).

Table S2. Number of events with more than 10 phases.

Table S3. Parameters used as input in HypoDD-ph2dt.

Table S4. HypoDD-PH2DT outputs. The HypoDD uncertainties histograms for each zone are represented in Figure S14.

Table S5. Relocation outputs.

Please note: Oxford University Press is not responsible for the content or functionality of any supporting materials supplied by the authors. Any queries (other than missing material) should be directed to the corresponding author for the paper.